Numeričko modeliranje procesa izgaranja različitih generacija biogoriva proizvedenog iz otpada biljnog podrijetla

Krajcar, Manuel

Master's thesis / Diplomski rad

2022

Degree Grantor / Ustanova koja je dodijelila akademski / stručni stupanj: **University of Zagreb, Faculty of Mechanical Engineering and Naval Architecture / Sveučilište u Zagrebu, Fakultet strojarstva i brodogradnje**

Permanent link / Trajna poveznica: https://urn.nsk.hr/urn:nbn:hr:235:238487

Rights / Prava: Attribution 4.0 International/Imenovanje 4.0 međunarodna

Download date / Datum preuzimanja: **2024-08-16**

Repository / Repozitorij:

Repository of Faculty of Mechanical Engineering and Naval Architecture University of Zagreb

UNIVERSITY OF ZAGREB
FACULTY OF MECHANICAL ENGINEERING AND NAVAL
ARCHITECTURE

MASTER'S THESIS

Manuel Krajcar

Zagreb, 2022.

UNIVERSITY OF ZAGREB
FACULTY OF MECHANICAL ENGINEERING AND NAVAL
ARCHITECTURE

NUMERICAL MODELLING OF COMBUSTION PROCESS OF DIFFERENT GENERATIONS OF BIOFUELS PRODUCED FROM PLANT-DERIVED WASTE

Mentor: Student:

Izv. prof. dr. sc. Milan Vujanović, dipl. ing.   Manuel Krajcar

Zagreb, 2022

Statement/ Izjava

I hereby declare that I have written this thesis independently using the knowledge acquired during my studies and the cited references.

Izjavljujem da sam ovaj rad izradio samostalno koristeći znanja stečena tijekom studija i navedenu literaturu.

Zagreb, 2022   Manuel Krajcar

SVEUČILIŠTE U ZAGREBU
FAKULTET STROJARSTVA I BRODOGRADNJE
Središnje povjerenstvo za završne i diplomske ispite
Povjerenstvo za diplomske ispite studija strojarstva za smjerove:
Procesno-energetski, konstrukcijski, inženjersko modeliranje i računalne simulacije i brodostrojarski

MASTER'S THESIS

Student:	**Manuel Krajcar**	JMBAG: 0035211890

Title of thesis in Croatian:
Numeričko modeliranje procesa izgaranja različitih generacija biogoriva proizvedenog iz otpada biljnog podrijetla

Title of thesis in English
Numerical Modelling of Combustion Process of Different Generations of Biofuels Produced from Plant-Derived Waste

Assignment description:

In order to meet the reduction of carbon dioxide (CO_2) emissions, biofuels are imposed as an alternative to conventional fuels in the transport sector. Biofuels produced from plant-derived waste have a positive impact on total carbon dioxide emissions, and a positive environmental impact on waste recovery. Blends of conventional fuel in the transport sector and a lower proportion of biofuels produced from plant-derived waste are already applicable in existing internal combustion engines without additional modifications. Computational fluid dynamics and chemical kinetics are commonly employed to investigate the combustion and autoignition properties of new fuels, including biofuels. Within the Master's thesis, it is necessary:

1. Present a brief overview and generation classification of biofuels in the transport sector;
2. Present in detail the technologies for production, characteristics, and chemical mechanisms of biofuels produced from the plant-derived waste;
3. Describe the fundamental equations of computational fluid dynamics and describe the equations of modelling chemical kinetics using the chemical mechanisms of fuel combustion;
4. Present numerical models used for numerical calculations;
5. Using the commercial software package "AVL FIRE ™ Workflow Manager" perform a detailed numerical simulation on the moving computational mesh of an industrial internal combustion engine;
6. Analyse and compare the obtained results with different biofuel / conventional fuel blend ratios against the available experimental data;
7. Based on computational simulations, quantify the reduced CO_2 emissions for each generation of biofuels.

All necessary literature, model description, input, and initial data for analysis will be obtained from the mentor and co-supervisor.

It is necessary to reference the used literature and any help received.

Thesis assigned:	Thesis submission date:	Thesis defence date:
March 5th, 2022	July 7th, 2022	July 18th –22th, 2022
Supervisor:		Committee Chair:
Izv. prof. dr. sc. Milan Vujanović		Prof. dr. sc. Tanja Jurčević Lulić

Table of contents

List of Figures

List of Tables

Nomenclature

Label	Unit	Description
A		Pre-exponential factor in Arrhenius law
A_S	m^2	Surface area
C		Model constant
c	kmol/m^3	Concentration
D	m	Droplet diameter
D_k	m^2/s	Diffusion coefficient
E	J/kg	Activation energy
e	J/kg	Specific energy
F_d	N	Drag force
f		Fuel mixture fraction
f_i	m/s^2	Resulting volume force
g		Residual gas mass fraction
k	m^2/s^2	Turbulent kinetic energy
k		Global reaction rate coefficient
L	m	Turbulence length scale
M	kg/kmol	Molar mass
P_k	m^2/s^3	Production of turbulent kinetic energy
p	Pa	Pressure
q	W/kg	Specific heat
R	J/molK	Ideal gas constant
r	m	Droplet radius
S_k		Source term
t	s	Time
T	K	Temperature
T	s	Turbulence time scale
u	m/s	Velocity
x_i	m	Coordinates
y		Mass fraction
α	W/m^{2}K	Coefficient of convective heat transfer
β		Coefficient in Arrhenius law
Γ	m^2/s	Diffusion coefficient
ε	m^2/s^3	Turbulent energy dissipation rate
ζ	m/s	Velocity scale ratio
κ		Chemical symbol for species k
Λ	m	Wave length
λ	W/mK	Thermal conductivity

μ	Pas	Dynamic viscosity
μ_t	Pas	Turbulent viscosity
ν		Stoichiometric coefficient
ρ	kg/m^3	Density
Σ	1/m	Flame surface density
σ_{ji}	N/m^2	Stress tensor
τ	N/m^2	Viscous stress
τ_a	s	Break-up time
υ	m^2/s	Kinetic viscosity
Ω	s	Wave growth rate
ω	kg/m^{3}s	Combustion source

Abbreviations

3D	Three Dimensional
B20	Diesel-Biodiesel mixture, 20 % volumetric share of Biodiesel
B50	Diesel-Biodiesel mixture, 50 % volumetric share of Biodiesel
BC	Boundary Conditiom
CA	Cranck Angle
CFD	Computational Fluid Dynamics
CO	Carbon Monoxide
CO$_2$	Carbon Dioxide
CPU	Central Proccessing Unit
D100	100 % volumetric share of Diesel
DDM	Discrete Droplet Method
ECFM-3Z	Extended Coherent Flame Model-3Z
FAME	Fatty Acid Methyl Ester
GGPR	General Gas Phasse Reaction
GHG	Greenhouse Gas
GSTM	General Specie Transport Model
ICE	Internal Combustion Engine
MD	Methyl Decanoate
MD9D	Methyl 9 Decenoate

NO$_x$ Nitrogen Oxide

NO   Nitrogen Monoxide

PM   Particulate Matter

RoHR   Rate of Heat Release

SCYLEN   Single Cylinder Engine

WCGO   Waste Coffee Ground Oils

Sažetak

U svrhu redukcije emisije ugljikovog dioksida, biogoriva se nameću kao alternativa konvencionalnim gorivima u transportnom sektoru. Biodizel je tip biogoriva dobiven iz otpada biljnog podrijetla. Radi zatvorenog ciklusa ugljikova dioksida, pokazala su pozitivan utjecaj na ukupne emisije ugljikova dioksida te imaju visoku korisnost oporabe otpada. Jedna od važnih prednosti biodizelskih goriva jest mogućnost miješanja s konvencionalnim dizelskim gorivom te njegova primjena u motorima s unutarnjim izgaranjem. Takve mješavine mogu se primjenjivati u motorima s unutarnjim izgaranjem uz minimalnu ili skoro nikakvu modifikaciju motora. Računalna dinamika fluida u kombinaciji s kemijskom kinetikom često se primjenjuje za analizu novih goriva, uključujući i biodizel. U ovom radu bit će dan kratki pregled i klasifikacija biogoriva, opisane fundamentalne jednadžbe računalne dinamike fluida te jednadžbe modeliranja izgaranje pomoću kemijskog mehanizma.

Također, provedene su numeričke simulacije izgaranja nekoliko generacija biodizela unutar softvera za računalnu dinamiku fluida AVL-FIRE™. Simulacije su validirane usporedbom dobivenih podataka za izgaranje n-heptana, surogata dizelskog goriva, s eksperimentalnim podacima dobivenih od strane AVL GmbH Graz. Analizirana su četiri tipa biodizela dobivena iz sirovina različitog biljnog podrijetla. Gorivo je analizirano u četiri radne točke te u različitim udjelima mješavine dizelskog goriva i biodizela.

Ključne riječi: Motor s unutarnjim izgaranjem, biogorivo, biodizel, RDF

Summary

In order to meet the reduction of carbon dioxide emissions, biofuels are imposed as an alternative to conventional fuels in the transport sector. Biofuel made from plant-derived waste, called biodiesel, has shown to positively impact total carbon dioxide emissions and have a positive environmental impact on waste recovery. One of the great advantages of biodiesel is its applicability in standard internal combustion engines when blended with conventional fuels. Such mixtures require very little or almost any additional modifications to the engines. Computational fluid dynamics combined with chemical kinetics is often employed to investigate combustion and auto-ignition properties of new fuels, including biofuels. This thesis will present a brief overview and generation classification of biofuels, describe the fundamental equations of computational fluid dynamics and the equations of modelling chemical kinetics using the chemical mechanism of fuel combustion.

Additionally, numerical simulations of the combustion process of different generations of biodiesel were performed in the computational fluid dynamics software AVL-FIRE™. Simulations were verified by comparing the obtained simulation data for n-heptane, a substitute for diesel fuel, to experimental data provided by AVL GmbH Graz. Biodiesels made from four different plant-derived feedstocks were compared under four operating conditions in various diesel-biodiesel blends.

Key words: Internal combustion engine, biofuel, biodiesel, CFD

Prošireni sažetak

Uvod

Kako se zakoni o redukciji štetnih plinova u motorima s unutarnjim izgaranjem konstantno pooštravaju te svijet teži k cilju dekarbonizacije i ugljične neutralnosti. Različita se goriva istražuju kako bi zamijenila ili barem umanjila primjenu fosilnih goriva u transportnom sektoru. Biodizel, motorno gorivo dobiveno iz sirovina biljnog ili životinjskog podrijetla, pokazalo se kao pogodna alternativa konvencionalnom dizelskom gorivu. Biodizel se dobiva procesom transesterifikacije metilnih estera masnih kiselina, gdje masne kiseline u reakciji sa određenim alkoholom kao katalizatorom formiraju biodizel te glicerol kao nusprodukt.

| Triglicerid | Alkohol | Biodizel | Glicerol |
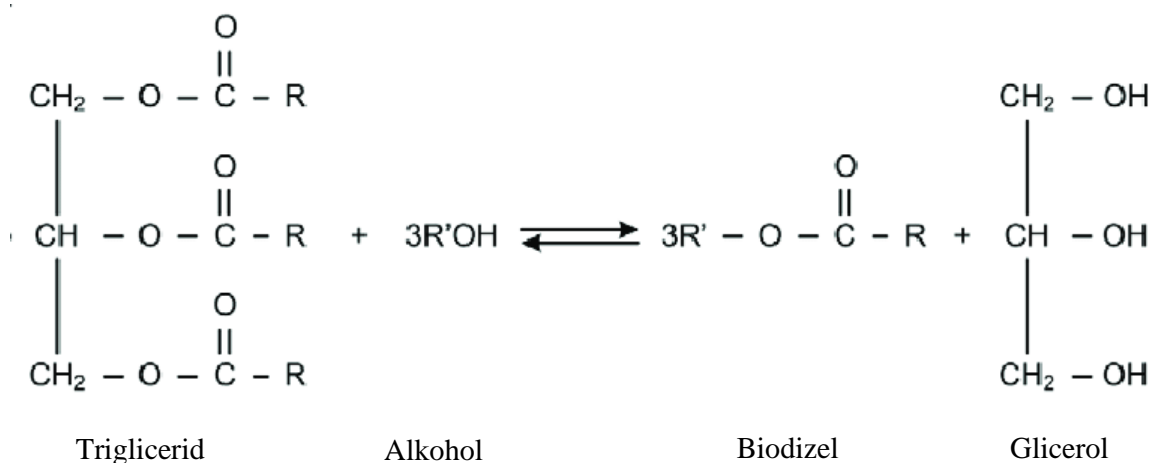
Slika 1   Proces transesterifikacije [1]

U današnjim dizel motorima, stopostotno biodizel gorivo i dalje nije primjenjivo kao takvo već ga se može pronaći u mješavini s konvencionalnim dizelskim gorivom u raznim volumnim postocima. Upravo je mogućnost korištenja biodizela u mješavini s dizelskim gorivom u postojećim ne modificiranim motorima njegova najveća prednost. Unatoč sličnim svojstvima samozapeljenja kao kod dizelskog goriva, eksperimenti su pokazali da korištenje stopostotnog biodizela u dizelskim motorima može narušiti njegov rad u smislu pojave raspadanja plastičnih cijevi i brtvenih elemenata te dilutacije motornog ulja koje može dovesti do utjecanja ulja u komoru za izgaranje [2].

Pomoću računalne dinamike fluida moguće je brzo i učinkovito prikazati proces izgaranja mješavina dizela i biodizela te prikazati učinak biodizela na smanjenje stakleničkih plinova. Cilj ovoga rada bio je prikazati proces izgaranja tri generacije biodizela iz različitih sirovina,

utjecaj sastava masnih kiselina tih sirovina na karakteristike izgaranja biodizela te usporedbu mješavina biodizela s konvencionalnim dizel gorivom.

Matematički model

Osnovni zakoni računalne dinamike fluida primijenjeni na proces izgaranja goriva u cilindru jesu zakon očuvanja mase, zakon očuvanja količine gibanja, zakon očuvanja energije te zakon očuvanja mase kemijskih vrsta:

$$\int_S \rho u_i n_i dS = -\frac{\partial}{\partial t}\int_V \rho dV \tag{I}$$

$$\int_V \frac{\partial}{\partial t}(\rho u_j)dV + \int_S \rho u_j u_i n_i dS = \int_V \rho f_j dV + \int_S \sigma_{ij} n_i dS \tag{II}$$

$$\int_V \frac{\partial}{\partial t}(\rho e)dV + \int_S \rho e u_i n_i dS = \int_V \rho f_i u_i dV + \int_S \sigma_{ij} u_i n_j dS - \int_S q_i n_i dS + \int_V S_e dV \tag{III}$$

$$\int_V \frac{\partial}{\partial t}(\rho y_k)dV + \int_S \rho y_k u_i n_i dS = \int_S \Gamma_k \frac{\partial y_k}{\partial x_i} n_i dS + \int_V S_k dV \tag{IV}$$

Model turbulencije

Turbulencija je nestacionarna i nelinearna pojava strujanja fluida pri visokim vrijednostima Reynoldsova broja. Gotovo sva strujanja u inženjerskoj praksi se smatraju turbulentnima uključujući i strujanja u cilindru. Turbulencija uvelike komplicira rješavanje jednadžbi u mehanici fluida te se njena pojava modelira pomoću Reynoldsovog osrednjavanja Navier-Stokesovih jednadžbi koji pretpostavlja osrednjavanje svih vrijednosti unutar domene. U ovom radu korišten je k-zeta-f model turbulencije koji se pokazao kao najprikladniji kod modeliranja turbulencije u procesu izgaranja.

Modeliranje spreja

U sklopu rada korišten je Euler Lagrangian pristup diskretnih kapljica kod kojeg se gorivo ubrizgava u komoru izgaranja u obliku skupine kapljica (parcela) koje imaju ista fizikalna svojstva dok se plinovita faza promatra kao kontinuum. Za kapljevitu fazu rješavaju se Lagrangeove jednadžbe očuvanja , a za plinovitu Eulerove. Kod modeliranja spreja korišteni su sljedeći podmodeli:

- Model raspadanja čestica → Wave

- Model isparavanja → Dukowicz
- Model turbulentne disperzije
- Model sile otpora → Schiller-Naumann
- Model međudjelovanja sa zidom → Walljet1

Modeliranje izgaranja

Modeliranje izgaranja izvršeno je pomoću kemijske kinetike, odnosno korištenjem kemijskog mehanizma. Kod ovakvog pristupa modeliranja izgaranja, za svaku kemijsku vrstu potrebno je izračunati po jednu jednadžbu očuvanja kemijske vrste u kojima se izvorski član modelira Arrheniusovom jednadžbom:

$$k = AT^{\beta} \, exp\left(-\frac{E}{RT}\right) \tag{V}$$

U kojoj je k globalni koeficijent brzine reakcije, A, β i E su predeksponencijalni faktor, eksponencijalni faktor ovisnosti o temperaturi te energija aktivacije. Vrijednosti A, β i E se određuju eksperimentalnim putem.

U ovom radu korišten je kemijski mehanizam razvijen na Sveučilištu Connecticut (UCONN) dobiven redukcijom mehanizma razvijenog od Nacionalnog laboratorija Lawerence Livermore (LLNL) koji se sastoji od 3299 kemijskih vrsta i 10806 kemijskih reakcija. Mehanizam je uspješno reduciran na 115 kemijskih vrsta i 460 kemijskih reakcija i razrađen je za simuliranje izgaranja biodizela putem dviju kemijskih vrsti, Metil dekanoata (MD) i Metil 9 decenoata (MD9D) koji predstavljaju surogate masnih kiselina koji sačinjavaju biodizel gorivo. MD predstavlja sve zasićene masne kiseline dok MD9D reprezentira sve nezasićene masne kiseline. Razlika zasićenih i nezasićenih masnih kiselina jest u broju dvostrukih veza između atoma ugljika. Najveći udio masnih kiselina u biodizelskom gorivu imaju*: Palmitinska, Stearinska, Oleinska, Linoleična te Linolenična* masna kiselina.

Numeričke postavke

Model motora na kojemu je temeljena proračunska mreža jest jedno cilindrični (SYCLEN) ispitni motor. Specifikacije motora i brizgaljke dane su u sljedećoj tablici:

Tablica 1   Specifikacije motora i brizgaljke

Motor		Brizgaljka	
Promjer cilindra	85 mm	**Broj sapnica**	8
Stapaj	94 mm	**Kut konusa spreja**	158°
Kompresijski omjer	16:1	**Talk ubrizgavanja**	1200-1600 bar
Položaj brizgaljke (od klipa)	3.8 mm	**Promjer mlaznice**	0.1 mm
Volumen	533.4 mm^3		

Proračunska mreža generirana je samo za osminu volumena cilindra iz razloga što brizgaljka ima osam sapnica. Zbog osne simetrije modelirana je samo jedna mlaznica na proračunskoj mreži sa selekcijama, koje je prikazana na sljedećoj slici.
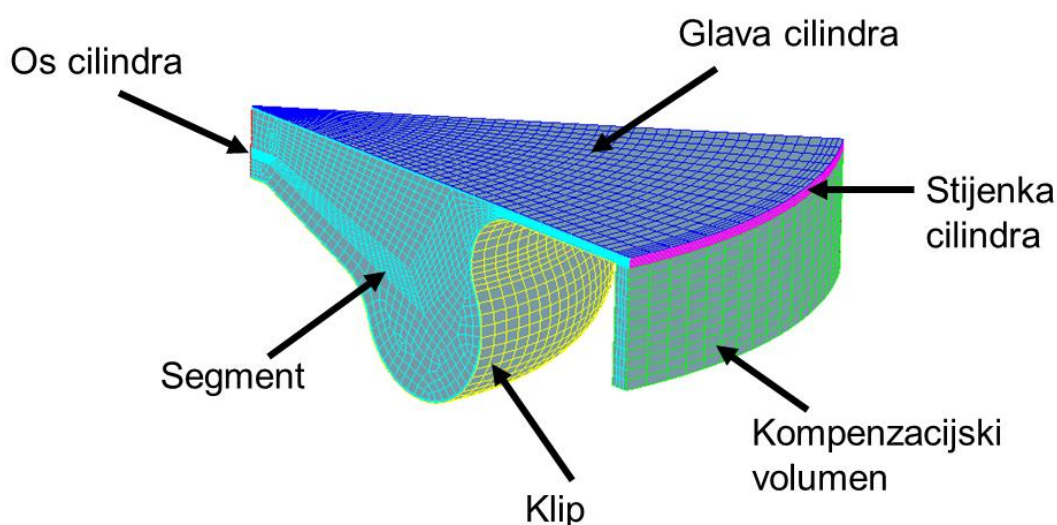
Slika 2   Proračunska mreža sa selekcijama za rubne uvjete

Postavljeni rubni uvjeti dani su u Tablica 2:

Tablica 2   Rubni uvjeti

Selekcija	Rubni uvjet
Klip	Tip: Zid Temperatura: 550 K
Stijenka cilindra	Tip: Zid Temperatura: 410 K
Os cilindra	Tip: Simetrija
Segment	Tip: Cirkulacija Ulaz/Izlaz
Kompenzacijski volumen	Tip: Zid Toplinski tok: 0 W/m^2
Glava cilindra	Tip: Zid Temperatura: 500 K

Kao što je spomenuto, promatrane su tri generacije biodizela, prvu generaciju predstavljala je sirovina kokosovo ulje, drugu generaciju predstavljali su ulje sjemenki rajčice te ulje iskorištenih zrna kave dok je treća generacija predstavljena mikroalgom Spirulina. Analizirane su mješavine u volumnom udjelu od 20 (B20) i 50 (B50) posto biodizela. Ulazna struktura goriva podešena je unutar programskog paketa AVL-FIRE™, gdje se dizel opisao surogatom n-heptanom (nC_7H_{16}), a biodizel MD i MD9D kemijskim vrstama:

Tablica 3   Maseni udio B20 dizel-biodizel mješavina

Kokosovo ulje				Ulje sjemenki rajčice			
Pravi sastav		**Modelirani sastav**		**Pravi sastav**		**Modelirani sastav**	
FAME	Maseni udio	Kemijska vrsta	Maseni udio	**FAME**	Maseni udio	Kemijska vrsta	Maseni udio
Laurinska	0.1742	**MD**	0.2849	**Laurinska**	/	**MD**	0.0558
Miristinska	0.0676			**Miristinska**	/		
Palmitinska	0.0332			**Palmitinska**	0.0393		
Stearinska	0.0099			**Stearinska**	0.0165		
Oleinska	0.0246	**MD9D**	0.0322	**Oleinska**	0.071	**MD9D**	0.2596
Linolna	0.0076			**Linolna**	0.1797		
Linolenska	/			**Linolenska**	0.0089		
n-Heptan	0.6829	**nC7H16**	0.6829	**n-Heptan**	0.6847	**nC7H16**	0.6847

WCGO				Spirulina mikroalga			
Pravi sastav		**Modelirani sastav**		**Pravi sastav**		**Modelirani sastav**	
FAME	Maseni udio	Kemijska vrsta	Maseni udio	**FAME**	Maseni udio	Kemijska vrsta	Maseni udio
Palmitinska	0.1134	**MD**	0.1365	**Palmitinska**	0.1709	**MD**	0.175
Stearinska	0.0231			**Stearinska**	0.0041		
Oleinska	0.0336	**MD9D**	0.1794	**Oleinska**	0.0166	**MD9D**	0.1413
Linolna	0.1428			**Linolna**	0.0518		
Linolenska	0.003			**Linolenska**	0.0729		
n-Heptan	0.684	**nC7H16**	0.684	**n-Heptan**	0.6838	**nC7H16**	0.6838

Tablica 4   Maseni udio B50 dizel-biodizel mješavina

Kokosovo ulje			
Pravi sastav		**Modelirani sastav**	
FAME	Maseni udio	Kemijska vrsta	Maseni udio
Laurinska	0.3571	**MD**	0.584
Miristinska	0.1385		
Palmitinska	0.0681		
Stearinska	0.0202		
Oleinska	0.0504	**MD9D**	0.066
Linolna	0.0156		
Linolenska	/		
n-Heptan	0.35	**nC7H16**	0.35

Ulje sjemenki rajčice			
Pravi sastav		**Modelirani sastav**	
FAME	Maseni udio	Kemijska vrsta	Maseni udio
Laurinska	/	**MD**	0.1146
Miristinska	/		
Palmitinska	0.0807		
Stearinska	0.0339		
Oleinska	0.1459	**MD9D**	0.5336
Linolna	0.3694		
Linolenska	0.0182		
n-Heptan	0.3518	**nC7H16**	0.3518

WCGO			
Pravi sastav		**Modelirani sastav**	
FAME	Maseni udio	Kemijska vrsta	Maseni udio
Palmitinska	0.233	**MD**	0.2804
Stearinska	0.0474		
Oleinska	0.0690	**MD9D**	0.3684
Linolna	0.2932		
Linolenska	0.0062		
n-Heptan	0.352	**nC7H16**	0.3512

Spirulina mikroalga			
Pravi sastav		**Modelirani sastav**	
FAME	Maseni udio	Kemijska vrsta	Maseni udio
Palmitinska	0.3508	**MD**	0.3591
Stearinska	0.0083		
Oleinska	0.034	**MD9D**	0.29
Linolna	0.1063		
Linolenska	0.1496		
n-Heptan	0.3509	**nC7H16**	0.3509

Navedene mješavine analizirane su u četiri slučaja, odnosno u četiri radne točke motora:

Tablica 5 Početni uvjeti

	Slučaj 1	Slučaj 2	Slučaj 3	Slučaj 4
Tlak, [Pa]	251800	252600	237700	241300
Gustoća, [kg/m^3]	2.08	2.08	1.991	2.002
Temperatura, [K]	422.5	425.1	416.1	419.9
Vrtloženje, [1/min]	5403	6869.1	5723.1	7096.2
Maseni udio [kg/kg]				
- O_2	0.2083	0.2038	0.2034	0.2128
- N_2	0.7631	0.7621	0.7621	0.7640
- CO_2	0.0196	0.0236	0.0239	0.0160
- H_2O	0.009	0.0105	0.0106	0.0072

Rezultati

U ovome radu prikazani su grafovi karakteristika izgaranja četiri radnih točaka motora za sve B20 i B50 dizel-biodizel mješavine. Zatim su prikazani trodimenzionalni rezultati temperature i masenog udjela dušičnih oksida unutar cilindra. Također, napravljena je relativna usporedba dva pristupa za kvantificiranje emisija ugljikovih dioksida iz motora s unutarnjim izgaranjem.
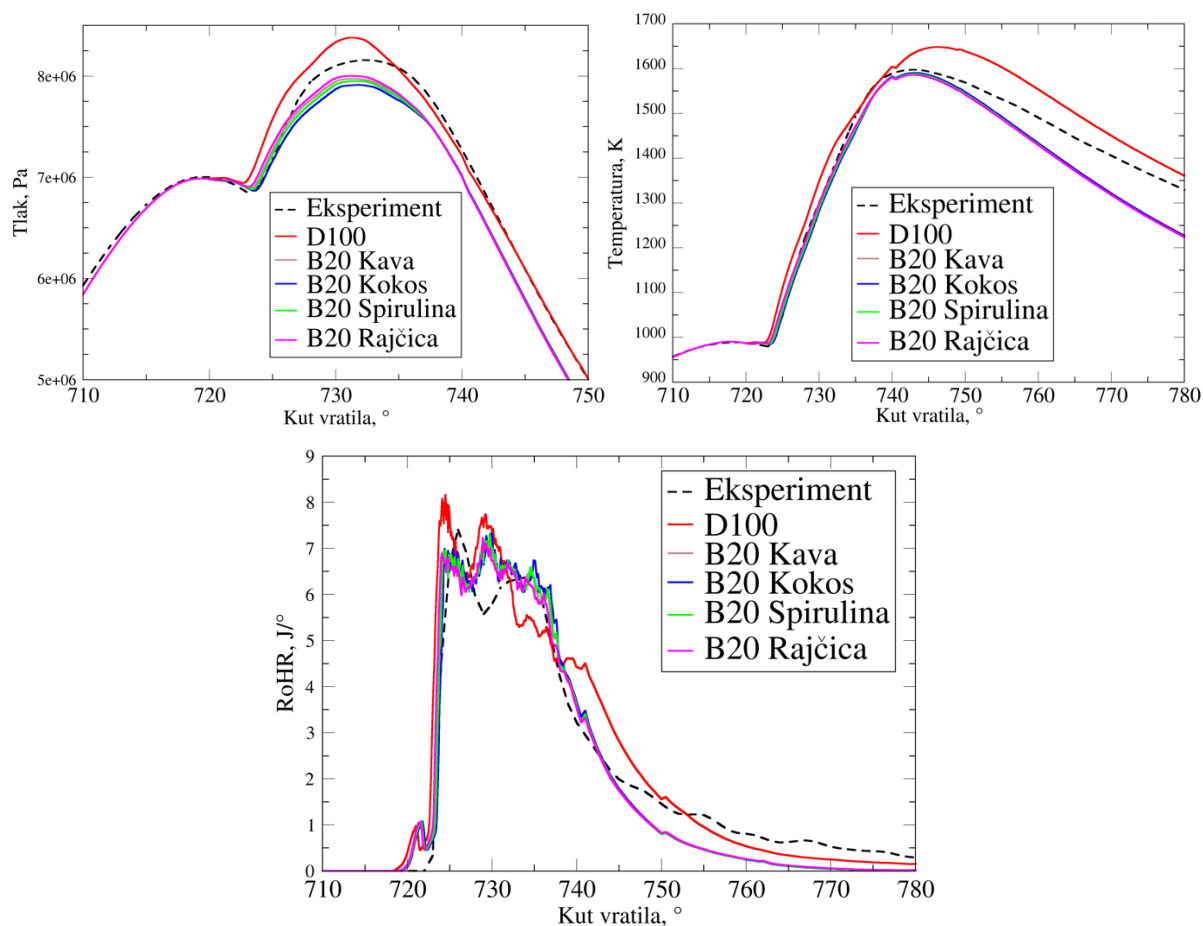
Slika 3 **Prosječni tlak, temperatura i brzina oslobađanja energije unutar cilindra za B20 dizel-biodizel mješavine – Slučaj 3**

Slika 3 prikazuje usporedbu tlaka, temperature te brzine oslobađanja energije za B20 mješavine biodizela sa dizelskim gorivom. Na slici je uočljivo odlično podudaranje u kompresijskom i ekspanzijskom procesu između kinetičkog mehanizma i eksperimentalnog mjerenja za konvencionalno dizelsko gorivo. Najveće razlike vidljive su u nešto kraćem vremenu zapaljenja dobivenom putem kinetičkog mehanizma koje se jasno vide u krivulji srednjeg tlaka unutar cilindra. Također mehanizam pokazuje nešto više vršne vrijednosti tlaka i brzine oslobađanja energije naspram izmjerenih veličina. Razlog tomu jest što se radi o reduciranom mehanizmu, gdje se dizelsko i biodizel gorivo opisuju pomoću surogatskih kemijskih vrsta.
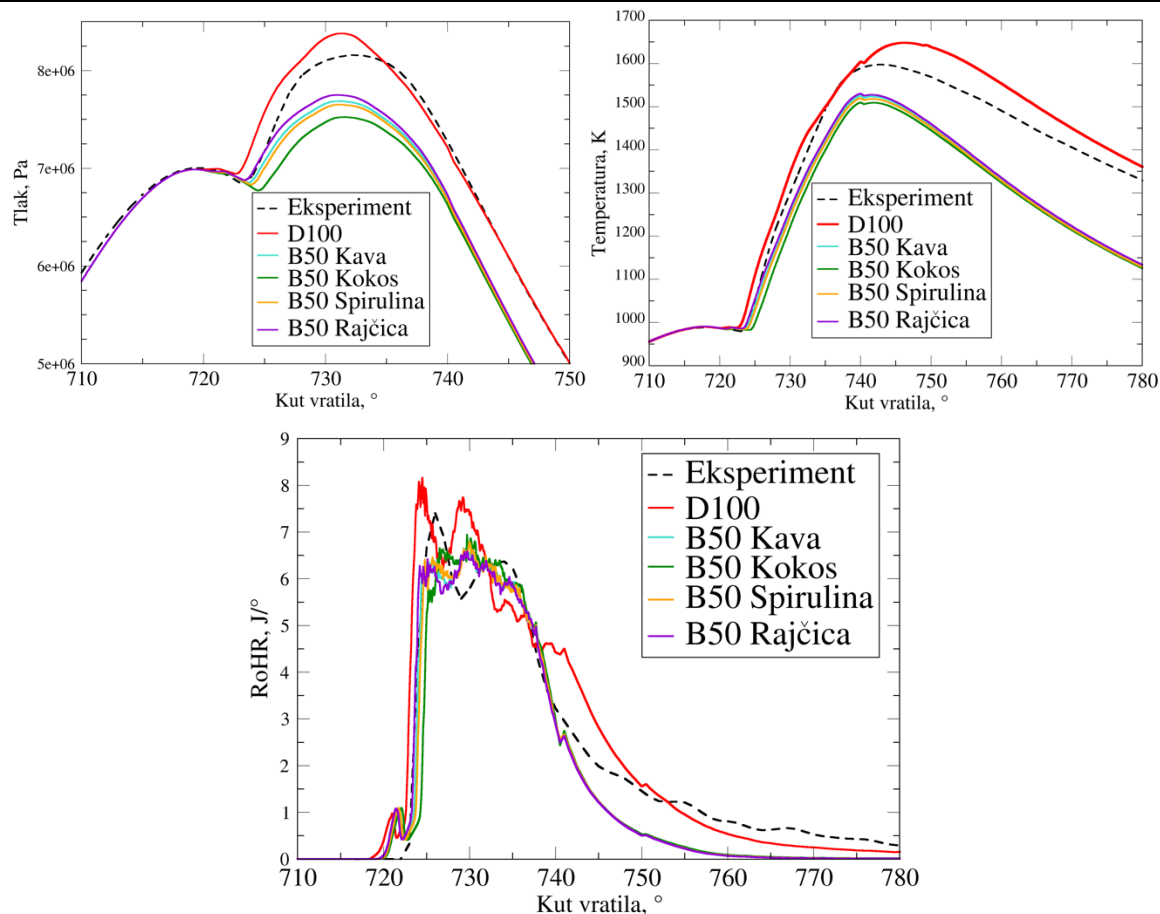
Slika 4　　　**Prosječni tlak, temperatura i brzina oslobađanja energije unutar cilindra za B50 dizel-biodizel mješavine – Slučaj 3**

Sve biodizelske mješavine imaju duže vrijeme zapaljenja smjese te niže vršne vrijednosti tlaka i brzine oslobađanja energije, razlika je posebno vidljiva kod većih udjela biodizela u mješavini goriva. Vidljivo je da mješavina ulja sjemenki rajčice od svih sirovina ima najkraće vrijeme zapaljenja te najveću vrijednost tlaka, dok mješavina kokosovog ulja ima najdulje vrijeme zapaljenja te najnižu vrijednost maksimalnog tlaka. Ulje iskorištenih zrna kave te ulje Spirulina mikroalge prikazuje iznimno slična ponašanja zbog gotovo istog udjela zasićenih i nezasićenih estera masnih kiselina. Može se zaključiti da veći udio nezasićenih kiselina, sa većim udjelom kisika u svojoj kemijskoj strukturi, pruža potpunije i efikasnije izgaranje. Međutim, zbog niže donje ogrjevne vrijednosti biodizel goriva, za postizanje istih vrijednosti oslobođene energije i tlaka u cilindru potrebna je veća količina ubrizganog goriva. Za postizanje jednake oslobođene energije kao kod konvencionalnog dizel goriva, potrebno je povećanje ubrizganog goriva od 14.4 % za B20 mješavine i 34 % za B50 mješavine. Usporedba utjecaja ubrizgane mase goriva na karakteristike izgaranja prikazana je na sljedećim slikama. Vidljivo je da je za obje mješavine, povećanjem mase ubrizganog goriva smanjeno vrijeme zapaljenja goriva te da je

gradijent tlaka, a ujedno i vršna vrijednost tlaka znatno porasla. Također vidljivo je i povećanje u brzini oslobađanja energije te je vršna vrijednost oslobođene energije također porasla. Pojava boljeg izgaranja može se pripisati većoj količini kisika koja se nalazi u masnim kiselinama biodizel goriva.
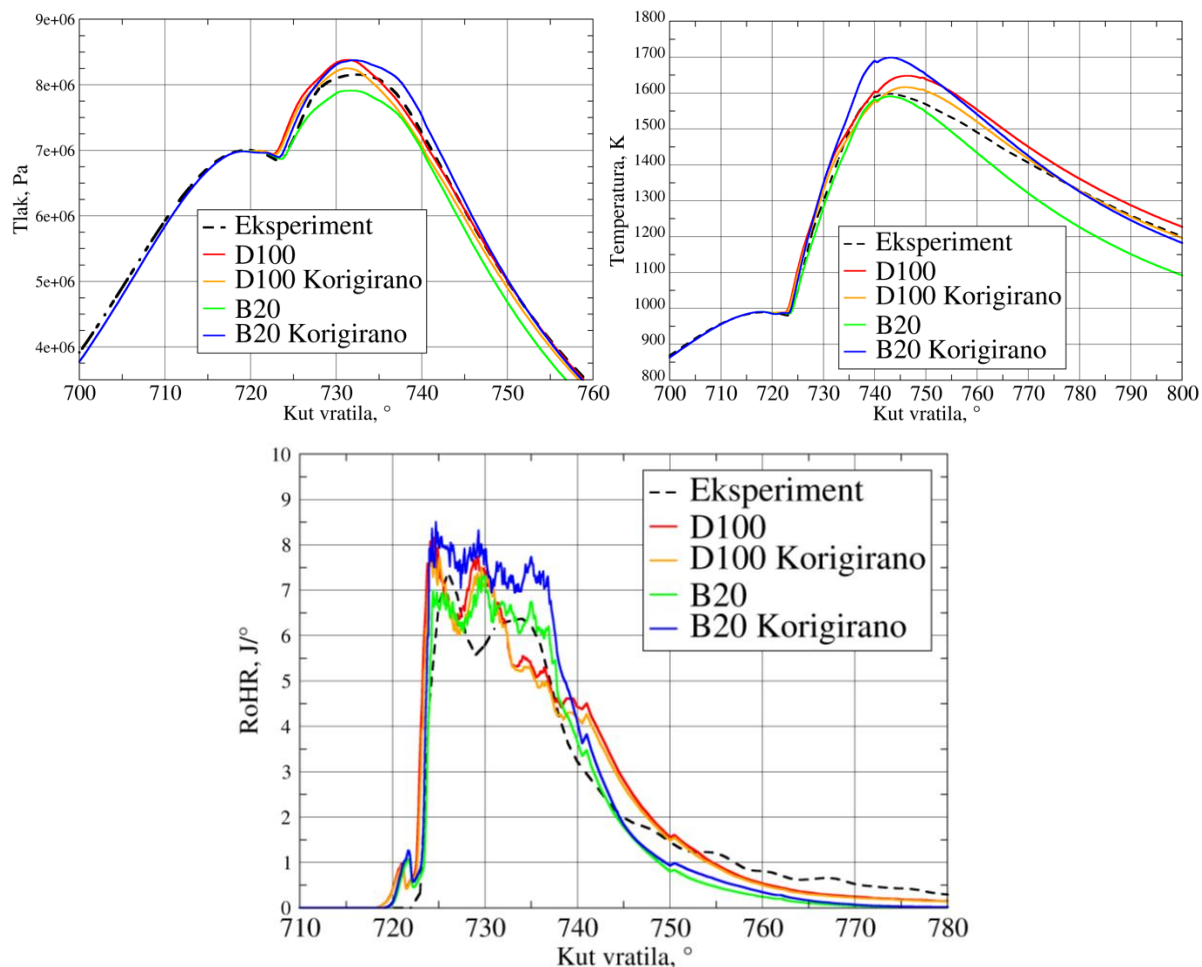
Slika 5   Tlak, temperatura i brzina oslobađanja energije B20 mješavine goriva sa različitim masama ubrizganog goriva – Slučaj 3
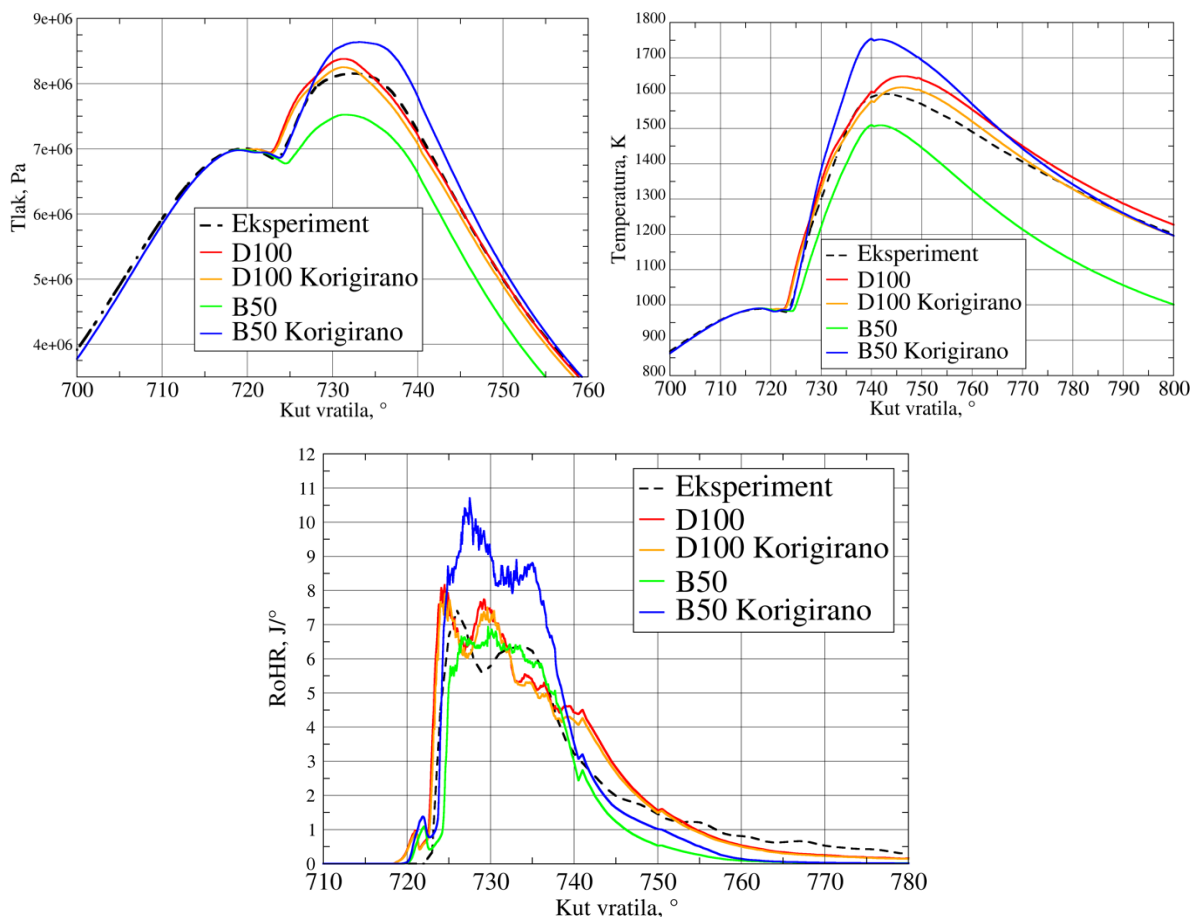
Slika 6 **Tlak, temperatura i brzina oslobađanja energije B50 mješavine goriva sa različitim masama ubrizganog goriva – Slučaj 3**

Analiza emisije ugljikova dioksida provedena je na dva načina, analizom ugljikova dioksida u ispušnim plinovima dobivenih putem CFD simulacija te metodom proračuna ugljikovog dioksida pomoći emisijskih faktora. Za proračun putem emisijskih faktora, iz literature su preuzete godišnje prosječne vrijednosti prijeđenog puta automobila s dizelskim motorom te njegova prosječna potrošnja. Vrijednosti su :

- Godišnji prijeđeni put od 19000 kilometara
- Prosječna potrošnja goriva 6.4 l/100 km

Na godišnjoj razini unutar Europske Unije utrošeno je 1034 kilograma dizelskog goriva po automobilu. Metodom emisijskih faktora računa se emisija ugljikova dioksida na godišnjoj razini putem sljedeće formule:

$$E_{CO_2} = A \cdot LHV \cdot EF_{fuel} \cdot OF \tag{VI}$$

Dok su vrijednosti CO_2 putem CFD pristupa dobivene na kraju jednog operativnog ciklusa motora s unutarnjim izgaranjem.

Tablica 6 Godišnja emisija CO_2

Gorivo	Meoda emisijskih fakora E_{CO_2}, t/godišnje	CFD pristup Maseni udio, kg/kg
D100	3.466	0.1094
B20 Kokos	2.936	0.0970
B50 Kokos	2.564	0.0870
B20 Rajčica	2.906	0.0970
B50 Rajčica	2.584	0.0888
B20 Kava	2.975	0.0973
B50 Kava	2.557	0.0880
B20 Spirulina	2.925	0.0969
B50 Spirulina	2.585	0.0878

Relativnom usporedbom naspram konvencionalnog dizelskog goriva (D100) uočene su redukcije kod svih biodizelskih sirovina. A razlika u dvama pristupa dana je u sljedećim grafovima.
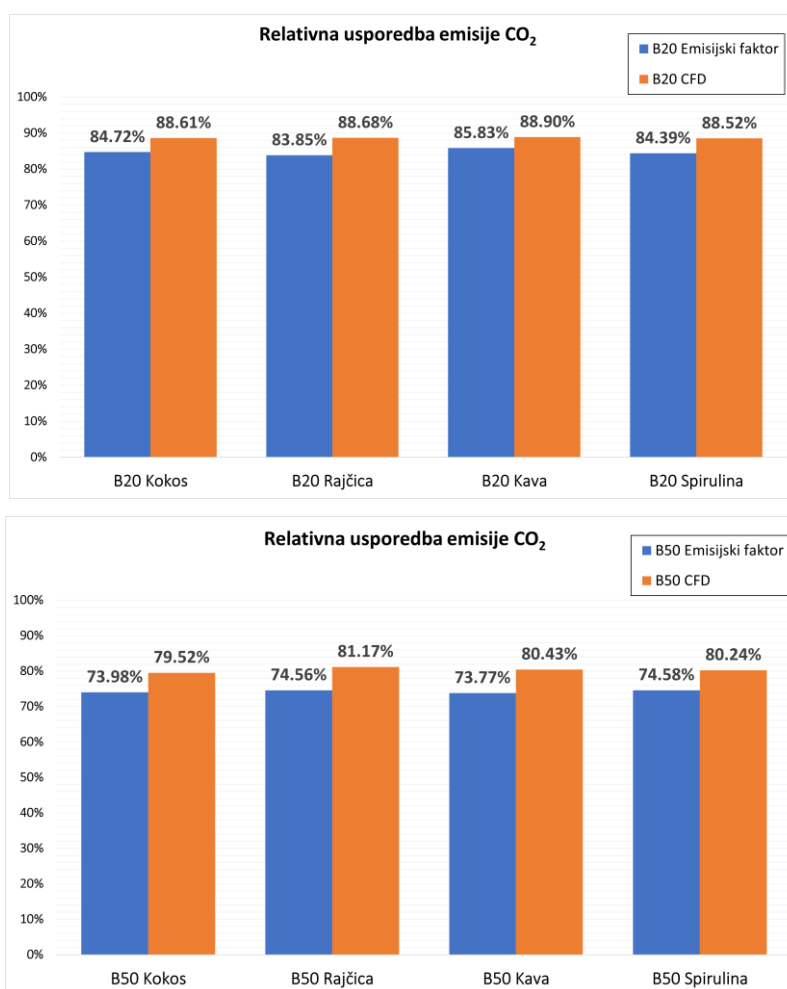
Slika 7   Relativne usporedbe B20 i B50 mješavina u emisijama CO_2

Proračunavanjem emisija putem emisijskih faktora, zapažene su veće redukcije CO_2 kod svih sirovina naspram CFD pristupa. Unatoč tomu, za potrebe računanja emisija ugljikova dioksida u vremenski kritičnim situacijama, proračun putem emisijskih faktora može dati dovoljno točna rješenja. Međutim, za detaljnije analize ispušnih plinova, CFD pristup može dati iznimno točna rješenja uzevši u obzir da se analize provode na razini jednog operativnog ciklusa motora.

1 INTRODUCTION

As the number of restrictions on Internal Combustion Engines (ICE) is rising steadily due to significant influence on the environment in terms of pollutant emissions, different fuels are being researched to replace or lower the usage of fossil fuels. Today's most used powering source in the transportation sector for ships, construction machinery, heavy trucks, and cars, diesel engines must constantly be improved to meet the strict regulations concerning pollutant emissions. Many pollutants are emitted from in-cylinder combustion in diesel engines, such as carbon dioxide (CO_2), particulate matter (PM), nitrous oxides (NO_x), and sulphides [3]. In 2017, the transport sector's greenhouse gas (GHG) emissions, including international aviation, increased by 242 Mt, or 28 %, compared to 1990 [4].

A solution to reducing emissions from diesel fuel combustion is the development of new carbon neutral fuels, such as biodiesel [5]. Biodiesel fuel consists of long-chain fatty acids esters derived from various vegetable oils and animal fats by transesterification, Figure 1. It is a chemical process used to convert fats (triglycerides)

into biodiesel along with glycerol as a by-product [6].
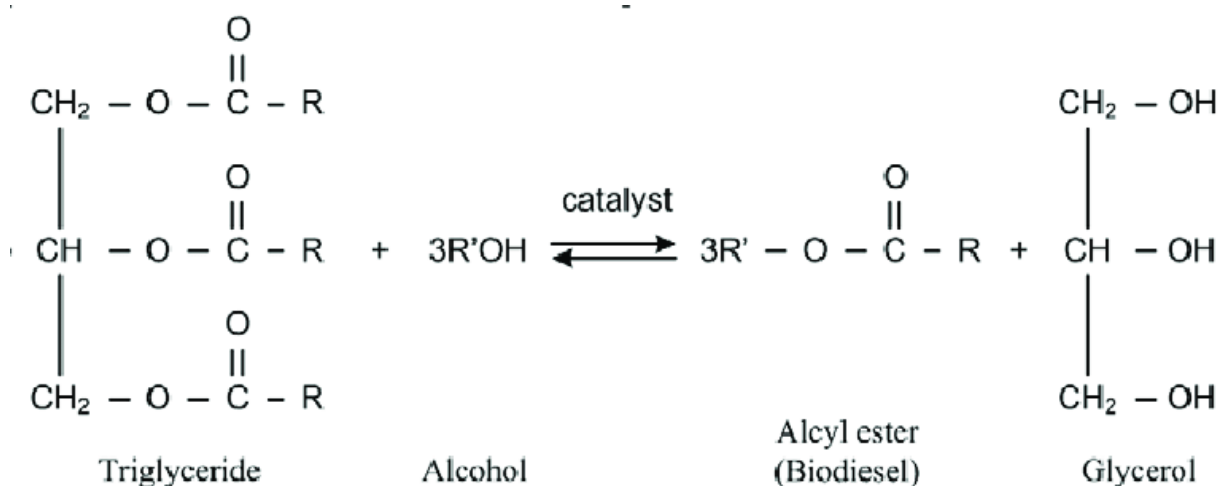
Figure 1   Transesterification reaction for biodiesel production [1]

Studies have shown that biodiesel utilization shows a decrease in hydrocarbons, carbon monoxide (CO), and PM, with a drawback in an increased NO_x production [7]. However, other researchers showed that the increase in NO_x is mainly due to biodiesel fuels used in unmodified diesel engines [8]. The authors in [9] compared microalgae biodiesel (Chaetoceros gracillis) to

soybean biodiesel and standard diesel. Their results showed lower CO, hydrocarbons, and NO_x emissions than the conventional diesel fuel.

Also, Rahman et al. showed that low volatility, high boiling point, density, and viscosity increase particle emission from microalgae biodiesel [10].

Over the years, technological improvements have made it possible to computationally analyze combustion processes in ICE using Computational Fluid Dynamics (CFD). Numerical simulations are widely used in engineering design and development [11]. By combining CFD analysis with experimental research, understanding complex and transient flow during the combustion process can be improved. Also, combining both experiments and CFD is a more time and cost-effective approach. The real-life experiments are expensive and complex due to the consistency of operational parameters [12]. Moreover, CFD has proved to be very helpful for in-cylinder pollutant emission analysis, as experimental analyses are known to be costly and troublesome to observe [13].

Recently, various CFD publications on biodiesel and biodiesel blends have been published. For instance, CFD software AVL-FIRE™ was combined with CHEMKIN code to analyze biodiesel-ethanol blends with various ethanol properties in a diesel engine [14]. Results showed a reduction of pressure inside the cylinder and thermal efficiency with increased ethanol share. The authors [15] combined AVL-BOOST™ with AVL-FIRE™ to examine various diesel-biodiesel blends on engine characteristics. Results showed a decrease in pollutant emissions such as PM, CO, hydrocarbon, and NO_x, which confirms the positive influence of biodiesel in ICE. A new model was implemented in AVL-FIRE™ [2], where simulations of diesel and diesel-biodiesel blends were performed. The results showed a decrease in NO_x emissions in the diesel-biodiesel fuel blends. The comparison of various sunflower biodiesel and diesel blends (D100, B10, B20 and B100) was investigated inside a single-cylinder heavy-duty engine in [13]. Results showed lower combustion intensity for biodiesel which affected the rate of heat release (ROHR). However, an average reduction in NO_x, CO and hydrocarbon emissions of 4.2 %, 8 %, and 20 % were observed. Authors of [16] investigated combustion and emission characteristics of biodiesel-diesel blends in a four-stroke diesel engine. Results showed an increase in NO_x emission with a higher biodiesel share. Compared to diesel, an increase of 8.6 %, 17.6 %, and 26.6 % was obtained for B10, B20, and B30. A new discrete-component vaporization model was developed specifically for the process of soot formation in biodiesel-diesel spray combustion [17]. The model is able to predict differences in the vaporization rates for various fuel components. Overall, model showed good agreement with the experimental

results in soot formation and the combustion temperatures. Lower soot formation and higher combustion temperatures than diesel fuel were obtained. Syngas and biodiesel were investigated in a compression engine powered in the dual fuel mode [18]. Combustion was analyzed using the Extended Coherent Flame Model-3Z (ECFM-3Z) in AVL-FIRE™. A higher syngas percentage showed decreased combustion efficiency but higher thermal efficiency. In addition, a higher syngas share reduces NO formation but increases CO and soot compared to plain biodiesel fuel.

Fossil fuels and biofuels contain varying blends of many hydrocarbons. Hence, detailed reaction mechanisms of numerous types of fuels, such as gasoline, jet, and diesel fuels, contain a significant number of species and reactions [19]. Regardless of rapid progress in computing power, applying such detailed mechanisms to computational simulations regarding the Central Processing Unit (CPU) time and memory requirements are still challenging. Thus, reduction of these complex mechanisms up to an appropriate size without impairing the computational fidelity is desired. An application of new reduction technique of various biomass-derived transportation fuel mechanisms resulted in numerous skeletal mechanisms [20]. A skeletal mechanism for biodiesel consisted of 177 species and 2904 reactions from a detailed mechanism consisting of 402 species and 16118 reactions. Results for ignition delay times showed a great match with the experimental data. Various authors executed mechanism reductions from a detailed kinetic mechanism made by Lawrence Livermore National Laboratory (LLNL). The mechanism consists of 3299 species and 10806 reactions. In performed research, a reduced biodiesel mechanism was developed, which can be used in CFD numerical studies of biodiesel applications [21]. The mechanism was reduced to 156 species and 589 reactions.

Additionally, researchers reduced the mechanism to 115 species and 460 reactions [22]. The reduced mechanism obtained a good prediction of combustion characteristics such as ignition delay, flame lift-off length, and equivalence ratio. Additional reduction of a detailed chemical mechanism for biodiesel obtained from the LLNL mechanism was performed in KIVA CFD software [23]. Starting mechanism consisted of 3299 species, and it was reduced to only 69 species making it usable for a three-dimensional (3D) CFD analysis in ICE. Biodiesel in the LLNL mechanism was described by two fuel surrogates, methyl decanoate (MD) and methyl-9-decenoate (MD9D), capable of representing the saturated and unsaturated methyl ester components of real biodiesel fuel. By altering the biodiesel Fatty Acid Methyl Ester (FAME)

composition, biodiesel from different origins and biodiesel-diesel blends can be defined and calculated with the chemical kinetic mechanism.

The aim of this thesis is to study the combustion properties and determine the emission formation of the different plant-derived biofuel generations using chemical kinetics and 3D CFD code. The CFD analysis can provide a sufficient insight into the physical and chemical phenomena of the combustion process, which can often not be visible from an experiment. In this work, plant-derived biofuels, are observed as blends with conventional fuel in the transport sector. After validating the chemical mechanism, such a detailed numerical calculation presents a valuable tool for quantifying pollutant emissions. Different generations of plant-derived biofuel are observed and compared, such as biofuel produced from coconut oil, tomato seed, waste coffee grounds oil, and Spirulina microalga.

2   MATHEMATICAL MODEL

Fundamental equations of continuum mechanics based on mass, momentum, and energy conservation laws are shown in this section. Also, models used to describe the process of combustion and heat release, such as turbulence, spray, and brake-up model, will be written out. Conservation laws are written in integral form in continuum mechanics, considering the total physical quantity inside the control volume. Furthermore, the conservation laws are written in integral form for fluid flows because the integral form is used in CFD calculations.

2.1   Mass conservation equation

$$\int_S \rho u_i n_i dS = -\frac{\partial}{\partial t} \int_V \rho dV \tag{1}$$

The integral form of mass conservation for a fixed control volume consists of two terms. The left term defines the mass flux rate through element boundary surface *S*, and it equals to the time rate of total mass change in the control volume *V*.

2.2   Momentum conservation equation

Conservation of momentum is derived from Newton's third law. The sum of the volume and surface forces acting on a fluid control volume element is equal to the time rate of momentum change of the fluid control volume element.

$$\int_V \frac{\partial}{\partial t}(\rho u_j) dV + \int_S \rho u_j u_i n_i dS = \int_V \rho f_j dV + \int_S \sigma_{ij} n_i dS \tag{2}$$

Eq(2) is written in index form where momentum is a vector consisting of three components *j* = 1, 2, 3. Each component describes the value of momentum in the Cartesian coordinate system and presents one scalar equation. The first term represents the time rate of momentum change of the control volume *V*. the Second term represents the sum rate of the flux through element boundary surface *S*. The third and fourth terms represent the resulting volume and surface forces acting on the control volume.

2.3 Energy conservation equation

Energy cannot be destroyed, it can only be converted from one form to another, and the system's total energy remains constant. Integral form of the energy conservation equation:

$$\int_V \frac{\partial}{\partial t}(\rho e)dV + \int_S \rho e u_i n_i dS = \int_V \rho f_i u_i dV + \int_S \sigma_{ij} u_i n_j dS - \int_S q_i n_i dS + \int_V S_e dV \qquad (3)$$

The first term represents the total energy change rate, while the second term represents the total energy transfer across the control volume boundaries. The first term on the right-hand side is the power of volume forces, and the second term is the power of surface forces acting on the control volume boundaries. Both terms are similar as in the momentum conservation equation. The third term on the right-hand side represents the heat transfer rate through the control volume boundaries. In the last term on the right-hand side, S_e denotes the volumetric distributed internal heat source due to radiation or chemical reactions. Eq(3) also represents the first law of thermodynamics since the first thermodynamic law is derived from the conservation of energy.

2.4 Specie mass conservation equation

In the combustion process, the conservation equations for each of the chemical species of interest are required. Opposite to the mass conservation equation, the source of chemical species inside the control volume can exist. For example, the source of chemical species from chemical reactions. The integral form of the energy conservation equation can be expressed as:

$$\int_V \frac{\partial}{\partial t}(\rho y_k)dV + \int_S \rho y_k u_i n_i dS = \int_S \Gamma_k \frac{\partial y_k}{\partial x_i} n_i dS + \int_V S_k dV \qquad (4)$$

where y_k is the mass fraction of the chemical species k (k is not notation index). The term y_k is defined as the ratio between the mass of chemical species k and total mass.

$$y_k = \frac{m_k}{m_{\text{total}}} \qquad (5)$$

The left-hand side terms are analogous to the terms found in the mass conservation equation. The first term on the right-hand side of Eq(4) is the diffusion term. The diffusion term is modelled by Fick's law. Furthermore, in the diffusion term, constant D_k is called diffusion coefficient, and it is an analogue to thermal conductivity coefficient in heat and mass transfer analogy.

2.5 Turbulence modelling

One of the essential predictions in engineering problems is efficient turbulent flow modelling. Fluid flow in ICE is considered turbulent due to its characteristically swirling flows. Therefore, an adequate turbulence model needs to be applied. Turbulence models are grounded on the Boussinesq assumption, which assumes that the Reynolds stress tensor can be modelled similarly as the viscous stress tensor. The k-zeta-f model is generally used in ICE simulations and was developed by Hanjalić, Popovac and Hadžiabdić [24]. Thus, it was chosen as a turbulence model for this thesis.

2.5.1 The k-zeta-f model

The model aims to improve the stability of the original $\overline{v^2} - f$ model by solving a transport equation for the velocity scale ratio $\zeta = \overline{v^2}/k$ instead of the velocity scale $\overline{v^2}$. The turbulent viscosity is obtained from:

$$\nu_t = C_\mu \zeta \frac{k^2}{\varepsilon} \tag{6}$$

Where C_μ is model constant, ζ is velocity scale ratio, k is turbulent kinetic energy and ε is the rate of turbulent energy dissipation.

Turbulent kinetic energy equation:

$$\rho \frac{Dk}{Dt} = \rho(P_k - \varepsilon) + \frac{\partial}{\partial x_j}\left[\left(\mu + \frac{\mu_t}{\sigma_k}\right)\frac{\partial k}{\partial x_j}\right] \tag{7}$$

Turbulent energy dissipation rate:

$$\rho \frac{D\varepsilon}{Dt} = \rho \frac{(C_{\varepsilon 1}^* P_k - C_{\varepsilon 2}\varepsilon)}{T} + \frac{\partial}{\partial x_j}\left[\left(\mu + \frac{\mu_t}{\sigma_k}\right)\frac{\partial \varepsilon}{\partial x_j}\right] \tag{8}$$

Velocity scale ratio:

$$\rho \frac{D\zeta}{Dt} = \rho f - \rho \frac{\zeta}{k} P_k + \frac{\partial}{\partial x_j}\left[\left(\mu + \frac{\mu_t}{\sigma_\zeta}\right)\frac{\partial \zeta}{\partial x_j}\right] \tag{9}$$

Elliptic relaxation function f can be written:

$$f - L^2 \frac{\partial^2 f}{\partial x_j \partial x_j} = \left(C_1 + C_2 \frac{P_k}{\varepsilon}\right)\frac{\left(\frac{2}{3} - \zeta\right)}{T} \tag{10}$$

Turbulent time scale T and length scale L are given by:

$$T = max\left(min\left(\frac{k}{\varepsilon}, \frac{a}{\sqrt{6}C_\mu |S|\zeta}\right), C_T\left(\frac{\upsilon}{\varepsilon}\right)^{\frac{1}{2}}\right) \tag{11}$$

$$L = C_L max\left(min\left(\frac{k^{\frac{3}{2}}}{\varepsilon}, \frac{k^{\frac{1}{2}}}{\sqrt{6}C_\mu |S|\zeta} \right), C_\eta \frac{v^{\frac{3}{4}}}{\varepsilon^{\frac{1}{4}}} \right) \qquad (12)$$

2.6   Spray modelling

Spray modelling is crucial for accurately describing mixing, ignition, combustion, and emission processes occurring in ICE. It simultaneously describes the multi-phase flow and solves conservation equations for both liquid and gas phases. Generally, the fuel is injected into the combustion chamber at high velocities in the form of a liquid jet, which then makes it disintegrate into small fragments due to high instabilities.
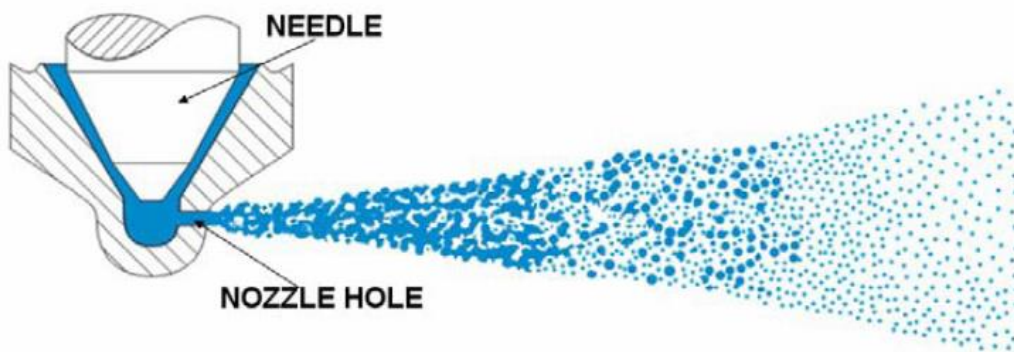
Figure 2   Spray structure [25]

The method used to solve practically all spray calculations in engineering problems today is called Discrete Droplet Method (DDM) or the Euler Lagrangian method. The method approximates spray droplets as groups of droplets (parcels) that exhibit the same properties. The liquid phase is calculated using the Lagrangian conservation equation, while the gas phase is described using the Eulerian approach.

Essential sub-models used in biodiesel injection are:

- Break-up model → Wave
- Evaporation model → Dukowicz
- Turbulence dispersion model
- Drag law model → Schiller-Naumann
- Wall interaction model → Walljet1

2.6.1 Break-up model

In the Wave break-up model, the growth of an initial perturbation on a liquid surface is linked to its wavelength and other physical and dynamic parameters of the injected fuel and the domain fluid.

There are two break-up regimes: low-velocity Rayleigh and high-velocity Kevin-Helmholtz. The Rayleigh regime is not representative of high-pressure injection systems, so it will not be used.

The radius reduction ratio of the drops is defined as:

$$\frac{dr}{dt} = -\frac{(r - r_{stable})}{\tau_a} \tag{13}$$

where τ_a is the break-up time of the model:

$$\tau_a = \frac{3.726 \, C_2 \, r}{\Lambda \Omega} \tag{14}$$

The constant C_2 is the second WAVE constant, and it corrects the breakup model. It varies from one injector to another.

r_{stable} represents the product droplet radius. It is a product of constant C_1 and the wavelength of the fastest-growing wave on the liquid surface.

$$r_{stable} = C_1 * \Lambda \tag{15}$$

The default value of C_1 is 0.61, and the wavelength Λ and wave growth rate Ω depend on the local flow properties:

$$\Omega = \left(\frac{\rho_d r^3}{\sigma}\right)^{-0.5} \frac{0.34 + 0.38 W e^{1.5}}{(1 + Oh)(1 + 1.4 T a^{0.6})} \tag{16}$$

$$\lambda_w = 9.02 r \frac{(1 + 0.450 h^{0.5})(1 + 0.4 T a^{0.7})}{(1 + 0.87 W e^{1.67})^{0.6}} \tag{17}$$

2.6.2 Evaporation model

Dukowicz evaporation model has the following assumptions for heat and mass transfer [26]:

- The spherical symmetry of droplets
- Quasi-steady gas film around the droplet
- Uniform droplet temperature at the drop diameter
- Uniform physical properties of the surrounding fluid

- Liquid-vapour thermal equilibrium on the surface of the droplet

The droplet temperature is defined by the following equation, which states that the energy conducted to the droplet either heats the droplet or supplies heat for vaporization:

$$m_d c_{pd} \frac{dT_d}{dt} = L \frac{dm_d}{dt} + \dot{Q} \tag{18}$$

The convective heat flux between the two phases:

$$\dot{Q} = \alpha A_s (T_\infty - T_s) \tag{19}$$

If the Nusselt number replaces the convective heat transfer coefficient, then the heat flux can be expressed as:

$$\dot{Q} = D_d \pi \lambda Nu (T_\infty - T_s) \tag{20}$$

The Nusselt number is obtained from the correlation proposed by Ranz and Marshal [27]

$$Nu = 2 + 0{,}6 Re_d^{\frac{1}{2}} Pr^{\frac{1}{3}} \tag{21}$$

2.6.3   *Drag law model*

The Shiller – Naumann drag model is used for calculating the drag from the gas phase on the droplets. The drag coefficient is calculated by [26]:

$$C_D = \begin{cases} 24 \dfrac{1 + 0{,}15 Re^{0.687}}{Re} ; & Re \leq 1000 \\ 0{,}44 ; & Re \geq 1000 \end{cases} \tag{22}$$

While the drag force is calculated by:

$$F_{di} = 0{,}5 \pi r^2 \rho C_D u_i^2 \tag{23}$$

2.6.4   *Wall interaction model*

Droplet behaviour at wall interaction depends on a couple of parameters such as droplet velocity, diameter, droplet properties, surface roughness and wall temperature. At low inlet velocities, the droplets tend to stick to the wall. However, when inlet velocities increase, a vapour layer is trapped underneath the droplet, causing the droplet to ricochet off the wall. There are two possible regimes at even higher droplet speeds, the spread or the splash regime. The spread regime makes the entire liquid spread across the wall, almost without normal velocity. In the splash regime, a part of the liquid remains near the wall surface while the rest is rebounded and broken into secondary droplets. In this work, the Walljet1 wall interaction

model was used. In this model, a vapour layer is formed around the droplets, promoting their reflection in interaction with the wall. However, this model does not consider the liquid wall film physics. The droplet diameter after the wall interaction can be calculated as a Weber's number function, where the reflection angle may differ $0 < \beta < 5$ degrees [26].

2.7 Combustion modelling

This thesis described the combustion process with the general gas phase reaction (GGPR) approach. Each fuel has its specific set of chemical reactions describing the combustion process. Chemical mechanism consists of elementary chemical reactions for each species individually. The reaction rates are calculated in the general form [28]:

$$\sum_{k=1}^{K} v'_{ki}\kappa_k \Leftrightarrow \sum_{k=1}^{K} v''_{ki}\kappa_k \ \ (i = 1, \dots, I) \tag{24}$$
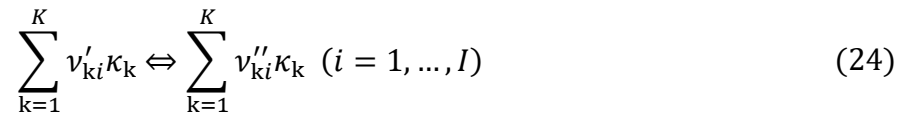
Where v represents stoichiometric coefficients of the reactants and products and κ is the chemical symbol for the species k.

The stoichiometric coefficient of species k in reaction i is defined as:

$$v_{ki} = v'_{ki} - v''_{ki} \tag{25}$$

while the reaction rate $\dot{q}_\iota$ of reaction is defined by the difference of forward and backward reaction rates:

$$\dot{q}_i = k_{f_i}\prod_{k=1}^{K}[c_{k,g}]^{v'_{ki}} - k_{r_i}\prod_{k=1}^{K}[c_{k,g}]^{v''_{ki}} \tag{26}$$

Where $c_{k,g}$ represents the molar concentration of species k.

The source term S_k from Eq(4) describing the species mass conservation can be modelled according to the Arrhenius law:

$$k = AT^{\beta} exp\left(-\frac{E}{RT}\right) \tag{27}$$

Where k is the global reaction rate coefficient, and E represents activation energy. The coefficients A, β and E are determined from experimental data. The coefficients A, β and E represent the pre-exponential factor, temperature dependence factor and activation energy. In this approach, the burning rate depends on the chemical kinetics while turbulent fluctuations are ignored. Inside the chemical reactions, species can originate as products or reactants. If the species is modelled as a reactant, it will be modelled as a sink in its transport equation. The

volume source S_k for a chemical species is expressed as a difference between all forward and backwards reactions, considering the concentration of chemical species in these reactions:

$$S_k = \frac{dc_k}{dt} \cdot M_k = \sum_1^m k_{m,f} \cdot c_m \cdot c_{oxy} - \sum_1^n k_{n,b} \cdot c_n \cdot c_{red} \tag{28}$$

Index m illustrates the total number of the forward reactions in which chemical species is a product, and index n is the total number of the backwards reactions in which chemical species is a reactant.

2.8 Species transport

Species transport was modelled with General Species Transport Model (GSTM). GSTM calculates Eq(4) for each chemical species k. The model has a list of all possible reactions in the combustion process, including intermediary reactions. For detailed chemical mechanisms, GSTM can be computationally demanding. Therefore, the transport equation does not have to be calculated for a specific chemical species, but its mass fraction can be obtained from stochiometric equations.

3   NUMERICAL SETUP

This chapter will overlook the necessary parameters for CFD simulations from the computational mesh, time step discretization, boundary and numerical setup, spray setup and injection rates, and the combustion model.

3.1   Engine and mesh information

The engine used for biodiesel combustion analysis is a Single CYlinder ENgine (SCYLEN), equipped with electro-hydraulic valve actuation and a ω- shaped piston. The schematics of an IC diesel engine combustion chamber is shown in Figure 3.
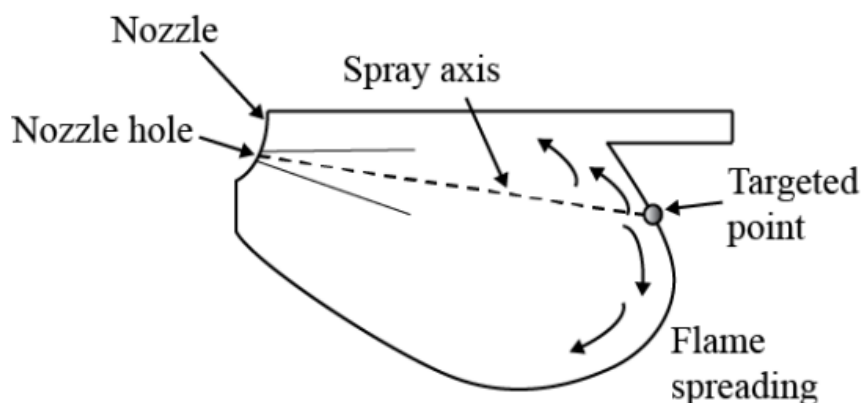
Figure 3   IC diesel engine combustion chamber [29]

Engine specifications are found in Table 1:

Table 1   Engine specifications

Engine data		Injector data	
Bore	85 mm	**Number of nozzle holes**	8
Stroke	94 mm	**Spray cone angle**	158°
Compression ratio	16:1	**Injection pressure**	1200-1600 bar
Nozzle location	3.8 mm	**Nozzle diameter**	0.1 mm
Displacement	533.4 mm^3		

The computational mesh used in this work was made for previous research by [2]. It contains two boundary layers surrounding the combustion chamber and a compensation volume at the piston rim. Due to axial symmetry, the mesh covers only a volume around one nozzle, and since the injector contains eight nozzles, only 1/8 of the cylinder volume was used. The mesh passed all the checks, and it has zero negative and non-orthogonal cells. As the domain is moving, computational mesh consists of 23 meshes generated from BDC to TDC. Cell information are shown in Table 2.

Table 2   Mesh information at TDC and BDC

|	TDC	BDC
Volume	472 cm^3	70.82 cm^3
Number of cells	65700	101150
Compression ratio	15	
No. of generated meshes	23	
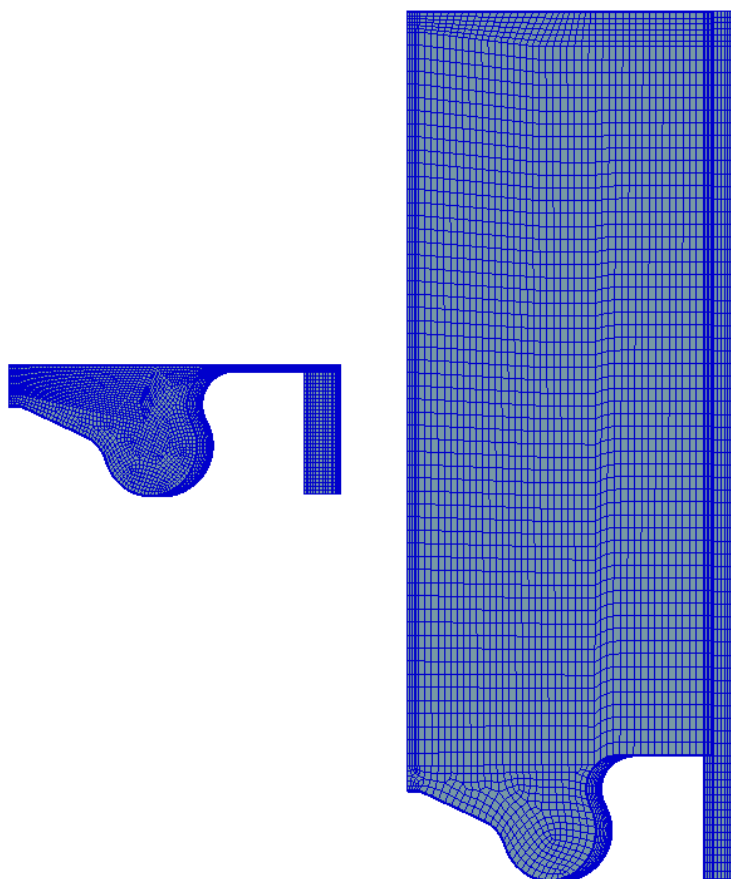
Figure 4   Mesh topology at TDC and BDC

3.2   Mesh dependency test

Three different meshes with the same block structure were tested. Meshes varied in the number of cells due to different cell sizes. The meshes had dependent cell sizes where up until 29.2 CA°, cell sizes were smaller so that the proper representation of the phenomena happening in TDC can be explored. Later, for higher CA°, cell sizes were larger to shorten the computational time. The specifications of the analysed meshes are given in the following table.

Table 3   Properties of analysed meshes

Mesh	Dependent cell size [mm]		No. of cells in TDC	No. of cells in TDC	No. of meshes
	0°CA	29.2°CA			
Coarse	0.6	1.2	49050	71775	23
Medium	0.5	1.0	65700	101150	23
Fine	0.4	0.8	92425	140975	27
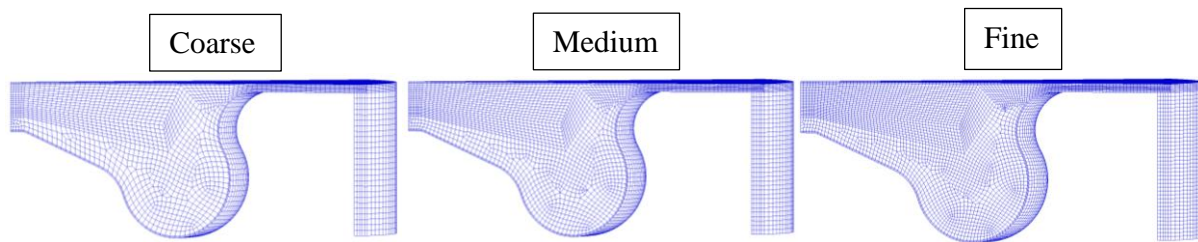
Figure 5   Computational meshes for the mesh dependency test

The comparison of the meshes was performed on Case 3 operating point (Table 6). The values of the in-cylinder mean pressure and the RoHR were observed. Obtained values are shown in Figure 6 and Figure 7.
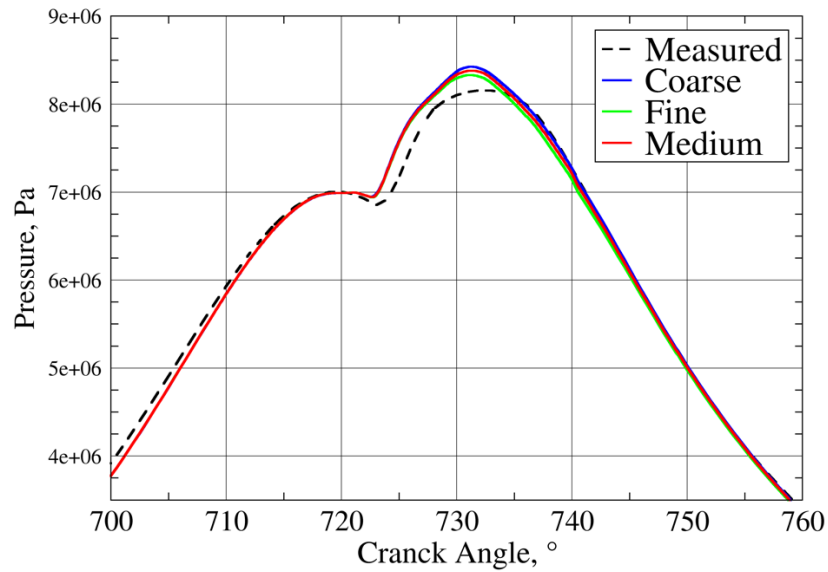
Figure 6   Cell size impact on in-cylinder mean pressure
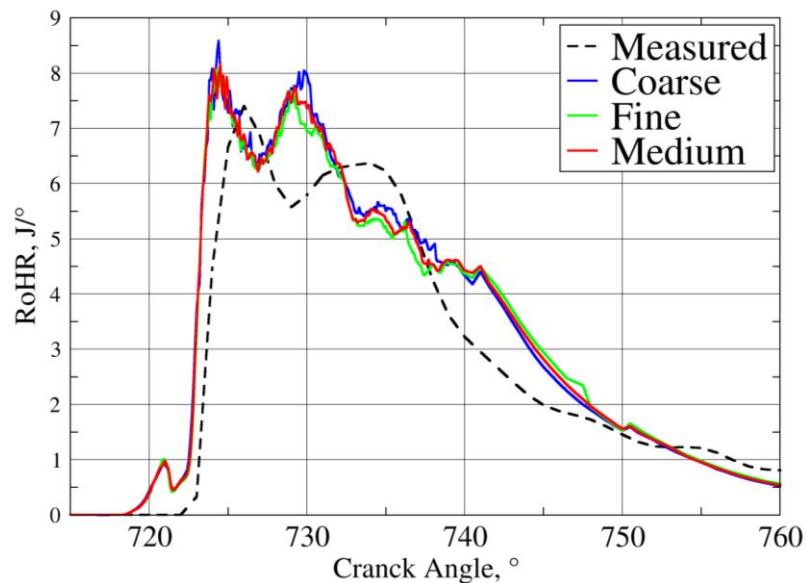
Figure 7   Cell size impact on RoHR values

It can be observed that there are minor differences in the tested meshes. There are no differences during the compression and the expansion period. Also, the ignition delay time is precisely the same for all the meshes. The most significant difference is in the peak values, where the coarse mesh shows slightly higher values than the fine and medium meshes, for which a negligible deviation was achieved. For this reason, in the following analysis, the medium mesh was used.

3.3   Time discretization

The run time for the combustion analysis was set in crank-angles (CA). The intake and the exhaust valve were closed during the working cycle period. Therefore, for different operating points start angle varied around 600 CA° depending on the time of valve closure. The end crank angle position is defined at 860 CA° for all operating points. An example of a time discretization is shown in Table 4.

Table 4   Simulation time step

Up to Crank-Angle, CA°	Time step, CA°
611	0.1
618	0.5
695	1
709	0.5
740	0.1
820	0.5
834	1
860	2

Minor time steps were used at the beginning of the simulations and during the fuel injection, ignition and combustion to acquire numerical stability.

3.4   Boundary conditions

Boundary conditions (BC) for the volume mesh were defined via boundary face selections. For every operating point, the same BC were used. Constant temperature BC was used for the cylinder head, the piston, and the liner. Symmetry BC is used for the axis. Since 1/8 of the volume was used, the segment boundary was periodic on both sides of the mesh, as shown in Figure 8. At the compensation volume walls, an adiabatic boundary condition was used. Table 5 shows the boundary conditions of the selected surfaces in Figure 8.
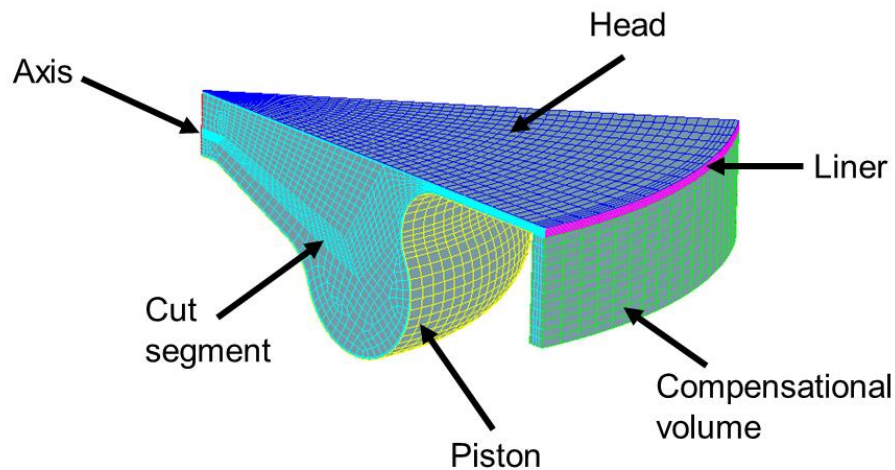
Figure 8   Computational mesh with defined selections

Table 5   Boundary conditions

Face	Boundary condition
Piston	Type: Wall Temperature: 550 K
Liner	Type: Wall Temperature: 410 K
Axis	Type: Symmetry
Cut segment	Type: Inlet/Outlet, Periodic
Compensation volume	Type: Wall Heat flux: 0 W/m^2
Head	Type: Wall Temperature: 500 K

3.5   Initial conditions

Pressure, density, temperature, swirl, and initial gas composition in ICE have to be set. When modelling combustion with GGPR, exact mass fractions of each species can be set. Initial values were used from acquired experimental data. This thesis analysed four different engine operating points, and its initial conditions are shown in Table 6.

Table 6   Initial conditions

	Case 1	Case 2	Case 3	Case 4
Pressure, Pa	251800	252600	237700	241300
Density, kg/m^3	2.08	2.08	1.99	2.00
Temperature, K	423	425	416	420
Swirl, 1/min	5403	6869	5723	7096
Mass fraction, kg/kg				
- **O_2**	0.2083	0.2038	0.2034	0.2128
- **N_2**	0.7631	0.7621	0.7621	0.7640
- **CO_2**	0.0196	0.0236	0.0239	0.0160
- **H_2O**	0.009	0.0105	0.0106	0.0072

3.6   Solver control

The under relaxation factors ensures smaller changes of the solution from one step to the next ensuring computational stability. By lowering the under relaxation factors, the solution changes very little between the steps, leading to a stable solution but prolonging the simulation time. On the contrary, if the under relaxation factors are too high, the solution changes excessively from one step to the next, leading to divergence. The defined under relaxation factors are shown in Table 7.

Table 7   Under relaxation factors

Equations	
Momentum	0.6
Pressure	0.3
Turbulent kinetic energy	0.4
Turbulent dissipation rate	0.4
Energy	1
Mass source	1
Viscosity	1
Scalar	0.8
Species transport equation	0.8

Concerning the differencing schemes, MINMOD Relaxed scheme was used for the momentum equation. The central differencing scheme was used for the continuity equation, whilst the upwind scheme was used for turbulence, energy, and scalar transport equations. For the pressure-velocity coupling, SIMPLE algorithm was used. The solution converged when the pressure and momentum residual decreased under the 10^{-4}.
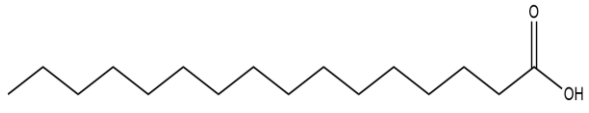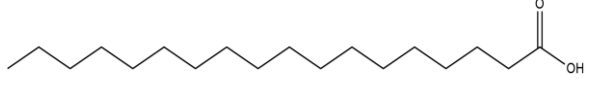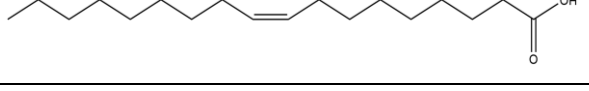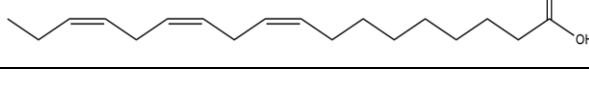
3.7 General Gas Phase Reactions

Chemical kinetic mechanisms are used to represent conventional and newly developed fuels in combustion devices like ICE [30]. The combustion process was modelled by The FIRE^{TM} General Gas Phase Reactions Module [28]. This model enables various types of chemical kinetic problems in 3D CFD. As mentioned before, detailed chemical kinetic mechanisms have shown to be ineffective for 3D transient combustion analysis due to high computational demands. Therefore, many researchers are performing reductions of these mechanisms to be implemented for 3D combustion analysis.

The kinetic mechanism used for biodiesel analysis in this thesis was developed by [22]. They performed a reduction of a detailed mechanism developed by LLNL. LLNL created a detailed kinetic mechanism for biodiesel consisting of two surrogate species, methyl decanoate (MD) and methyl-9-decenoate (MD9D) [31]. The two surrogates can efficiently represent saturated and unsaturated methyl esters of biodiesel. Using various mechanism reduction methods, the authors reduced the mechanism from 3299 species and 10806 reactions to 115 species and 460 reactions, respectively.

3.8 Fuel composition

The primary biodiesel production method is transesterification. It is a reaction of oils or fat with alcohol in which esters and glycerol (as a by-product) are produced. However, various biodiesel production methods are being developed [32]. Biodiesel is comprised of multiple fatty acid methyl esters, of which five main esters are obtained from *Palmitic*, *Stearic*, *Oleic*, *Linoleic,* and *Linolenic* acid, [33]. Fatty acids can be divided into saturated fatty acids and unsaturated fatty acids. The main difference is in the type of bonds. Saturated fatty acids have hydrocarbon chains connected by single bonds only, while unsaturated fatty acids have one or more double bonds. Palmitic and Stearic acids are a type of saturated fatty acids which can be seen from their chemical structure as they do not contain any double bonds. On the other hand, Oleic, Linoleic and Linolenic acids are all unsaturated fatty acids as they contain one, two and three double bonds, respectively.

Table 8   Fatty acid methyl esters

Fatty acids	Molecular formula	Chemical Structure
Palmitic acid (C16:0)	$C_{16}H_{32}O_2$	
Stearic acid (C18:0)	$C_{18}H_{36}O_2$	
Oleic acid (C18:1)	$C_{18}H_{34}O_2$	
Linoleic acid (C18:2)	$C_{18}H_{32}O_2$	
Linolenic acid (C18:3)	$C_{18}H_{30}O_2$	

First, second, and third-generation biodiesels were analysed in this thesis. Coconut oil represents the first-generation biofuel as it is considered an edible feedstock [34]. Two second-generation fuels are represented by tomato-seed oils [35] and waste coffee ground oils (WCGO) [36]. The third-generation biofuels are composed of microalgal feedstock. Spirulina microalga was analysed, and its composition was obtained from [37]. Only the fatty acids with the highest share were considered for the combustion analysis, while the other acids with a negligibly small share were neglected. For tomato-seed oil and spirulina microalgae, the highest percentage of fatty acid methyl esters have the previously mentioned *Palmitic*, *Stearic*, *Oleic*, *Linoleic,* and *Linolenic* methyl esters, while coconut oil has a high share of *Lauric* (C12:0*)* and *Myristic* (C14:0) fatty acids. The composition of analysed biodiesels is shown in Figure 9.
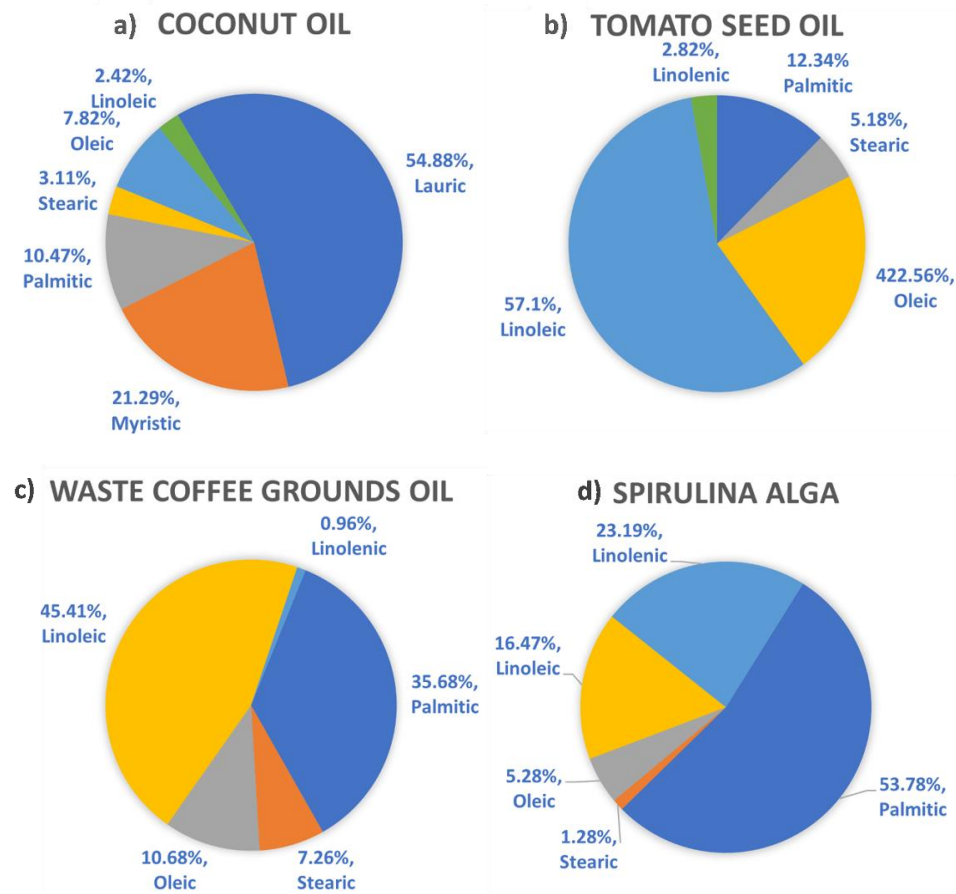
Figure 9   Volumetric composition of FAME in Coconut oil (Figure 3a), Tomato seed oil (Figure 3b), WCGO (Figure 3c), Spirulina microalga (Figure 3b)

3.9   Spray setup

Firstly, the fuel properties must be set up. Biodiesel properties were described with FAME-R, while DIESEL-D1 will represent the diesel properties. The temperature of the injected fuel was experimentally measured, and its value was set to 320 K. The exact fuel blend ratio and fuel composition have to be defined from the species found in the kinetic mechanism. As mentioned, the chosen mechanism represents FAME via the two surrogate species. The saturated FAMEs are represented by MD, and the unsaturated by MD9D, respectively.

B100 and high concentration FAME diesel blends cannot be used in ICE without a substantial risk of oil quality deterioration and the clogging of particulate filters and dissolving materials. Therefore, many world regions have limits on maximum FAME concentration in diesel fuels for conventional vehicles, like Europe, where the maximum FAME concentration in diesel is limited to 7 % by EN590. Nevertheless, higher FAME concentrations can be used in fleet operations like city busses, taxis, or heavy-duty transport like trucks, tractors, and marine diesel

engines. This higher FAME concentrated fuels are standardized in Europe under norms EN 16734, EN 16709 or EN 14214 for B10, B20 and B30 blends, respectively. For this reason, mixtures with higher FAME share of B20 and B50 will be analysed in SYCLEN. The B20 and B50 blends composition for the analysed feedstocks are shown in Table 9 and Table 10.

Table 9   Mass fraction of B20 biodiesel-diesel blends

Coconut oil					Tomato seed oil			
Real composition		**Model composition**			**Real composition**		**Model composition**	
FAME	Mass fraction	Chemical specie	Mass fraction		**FAME**	Mass fraction	Chemical specie	Mass fraction
Lauric	0.1742	**MD**	0.2849		**Lauric**	/	**MD**	0.0558
Myristic	0.0676				**Myristic**	/		
Palmitic	0.0332				**Palmitic**	0.0393		
Stearic	0.0099				**Stearic**	0.0165		
Oleic	0.0246	**MD9D**	0.0322		**Oleic**	0.071	**MD9D**	0.2596
Linoleic	0.0076				**Linoleic**	0.1797		
Linolenic	/				**Linolenic**	0.0089		
n-Heptane	0.6829	nC_7H_{16}	0.6829		**n-Heptane**	0.6847	nC7H16	0.6846

WCGO					Spirulina microalga			
Real composition		**Model composition**			**Real composition**		**Model composition**	
FAME	Mass fraction	Chemical specie	Mass fraction		**FAME**	Mass fraction	Chemical specie	Mass fraction
Palmitic	0.1134	**MD**	0.1365		**Palmitic**	0.1709	**MD**	0.175
Stearic	0.0231				**Stearic**	0.0041		
Oleic	0.0336	**MD9D**	0.1795		**Oleic**	0.0166	**MD9D**	0.1413
Linoleic	0.1428				**Linoleic**	0.0518		
Linolenic	0.003				**Linolenic**	0.0729		
n-Heptane	0.684	nC7H16	0.684		**n-Heptane**	0.6838	nC7H16	0.6837

Table 10   Mass fraction of B50 biodiesel-diesel blends

Coconut oil				Tomato seed oil			
Real composition		**Model composition**		**Real composition**		**Model composition**	
FAME	Mass fraction	Chemical specie	Mass fraction	**FAME**	Mass fraction	Chemical specie	Mass fraction
Lauric	0.3571	**MD**	0.584	**Lauric**	/	**MD**	0.1146
Myristic	0.1385			**Myristic**	/		
Palmitic	0.0681			**Palmitic**	0.0807		
Stearic	0.0202			**Stearic**	0.0339		
Oleic	0.0504	**MD9D**	0.066	**Oleic**	0.1459	**MD9D**	0.5336
Linoleic	0.0156			**Linoleic**	0.3694		
Linolenic	/			**Linolenic**	0.0182		
n-Heptane	0.35	**nC7H16**	0.35	**n-Heptane**	0.3518	**nC7H16**	0.3518

WCGO				Spirulina microalga			
Real composition		**Model composition**		**Real composition**		**Model composition**	
FAME	Mass fraction	Chemical specie	Mass fraction	**FAME**	Mass fraction	Chemical specie	Mass fraction
Palmitic	0.233	**MD**	0.2804	**Palmitic**	0.3508	**MD**	0.3591
Stearic	0.0474			**Stearic**	0.0083		
Oleic	0.0690	**MD9D**	0.3684	**Oleic**	0.034	**MD9D**	0.29
Linoleic	0.2932			**Linoleic**	0.1063		
Linolenic	0.0062			**Linolenic**	0.1496		
n-Heptane	0.352	**nC7H16**	0.3512	**n-Heptane**	0.3509	**nC7H16**	0.3509

For each specific case, different amounts of fuel in different CA° were injected. As only 1/8 of the cylinder was analyzed, only 1/8 amount of fuel was injected into the domain. The amount of fuel and the beginning of injection for each case is shown in Table 11.

Table 11   Injection timing and amount of injected fuel

	Case 1	**Case 2**	**Case 3**	**Case 4**
Injected mass, µg	3.38	3.39	3.39	3.37
Injection timing, CA°				
- **Start**	713.5	709.3	715.8	712.6
- **Stop**	734.8	732.4	735.6	732.4

After the liquid properties were set and the amount of injected fuel defined, the definition of spray submodels was required. The used submodels are shown in Table 12.

Table 12   Spray submodels

Drag law model	**Schiller Naumann**
Particle interaction model	Schmidt
Wall interaction model	Walljet1
Evaporation model	Multi-component
Breakup model	Wave

Next, the particle introduction from the nozzle followed. Three parameters are required to be defined. First, the number of different particle sizes introduced per time step and ring (NSIZES). The number of radial parcel release locations on each injection hole (NINTRO) and the number of circular parcel release locations on each ring (NCIRCD). The total number of parcels being introduced each time step equals to NSIZES×NINTRO×NCIRCD.

Table 13   Particle introduction from nozzle

NSIZES	3
NINTRO	3
NCIRCD	3

The injector geometry was defined from the SCYLEN. Table 14 shows the injector data input necessary to perform numerical simulations.

Table 14   Injector data

Position	**(0, 0, -3.8) mm**
Direction	(0, 0, 1)
Nozzle hole diameter	0.1 mm
Nozzle diameter at hole centre position	4 mm
Spray delta angle 1	158°
Half outer cone angle	7.5°

The spray delta angle 1 represents the double angle between the spray axis and the nozzle axis, while the half outer cone angle is defined as the angle between the nozzle hole axis and the widest parcel trajectory.

Along with all the necessary numerical setup, the following assumptions were made:

- Ideal gas properties for the components in the cylinder: Prandtl number, Pr=0.9, Schmidt number, Sc=0.7

- Compressible flow

- Viscid fuel (WAVE C3=1)

- No interaction between the droplets

4   RESULTS AND DISCUSSION

The following chapter shows the results of different diesel-biodiesel blends made of three different generation feedstocks. Combustion characteristics such as in-cylinder pressure, ROHR and internal temperature were observed and compared to simulations of conventional diesel fuel and the obtained experimental measurements. Furthermore, a 3D comparison of temperature fields and NO_x shares in the combustion chamber were analysed.

4.1   B20 Blends

As seen in Table 9, the FAME composition of analysed biodiesel fuels varied depending on the plant-derived feedstock. For example, coconut oil is shown to have the highest share of shorter carbon chain saturated fatty acids. Conversely, tomato-seed oil has the highest share of longer carbon chain unsaturated fatty acids. WCGO and Spirulina blends have a somewhat similar share but of opposite FAME, meaning that the content of the saturated fatty acids of WCGO blends is like the unsaturated content of Spirulina blend.

Firstly, when comparing the experimental measures to the modelled (D100) diesel, great accordance can be seen across all the operating points during the compression and expansion strokes. However, when ignition commences, D100 tends to ignite sooner and reaches higher pressure values. This can be attributed to D100 being depicted by a surrogate n-heptane.

The obtained results of the pressure distribution inside the cylinder for B20 blends show lower pressure values for all the diesel-biodiesel mixtures compared to the conventional fuel. An approximate 5 % reduction in peak pressure for B20 blends compared to D100 is obtained in Case 1. A comprehensive comparison between the analysed feedstock will be given for each case separately.
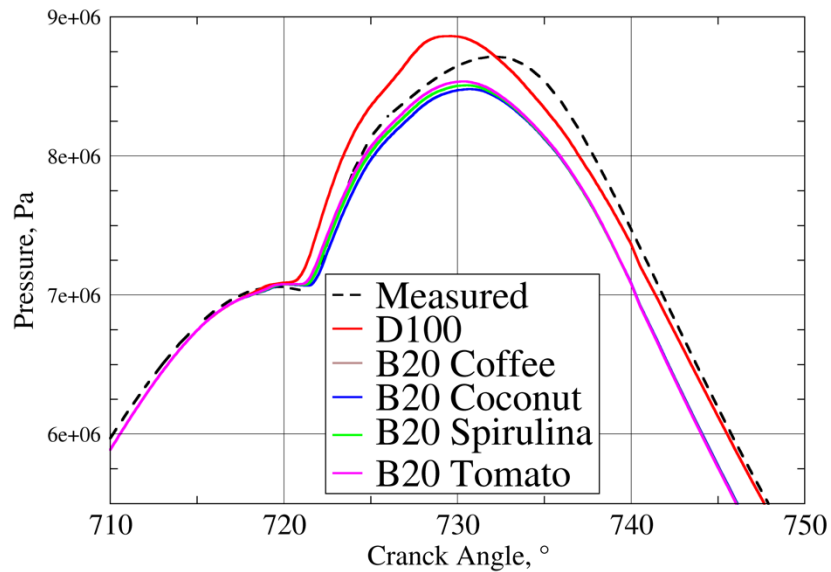
Figure 10 In-cylinder pressure distribution of B20 blends – Case 1

When comparing the pressure values of different feedstock blends, very similar values are obtained. During the ignition phase, the coconut blend ignited the last while the tomato-seed mixture ignited first. Spirulina and WCGO blends are in between the coconut and the tomato blends with their almost equal composition of saturated and unsaturated FAME. Due to such similar composition, no significant difference between the two feedstocks is observed as their peak values and ignition delay time are practically identical. Behaviour in Case 1 can lead to the conclusion that the higher share of unsaturated fatty acids can lead to sooner ignitions and higher pressures. Moreover, FAME composition showed no influence on the in-cylinder pressure during the compression and expansion strokes.
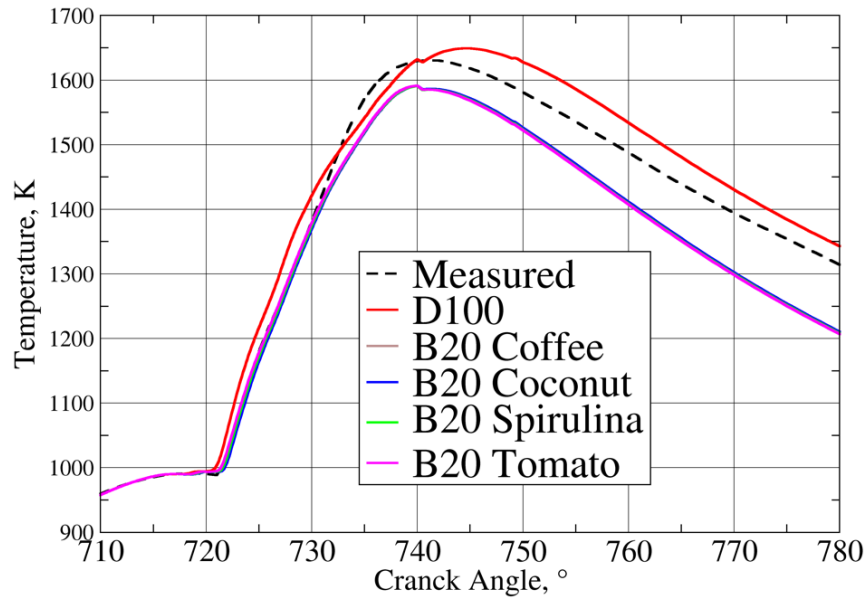
Figure 11 In-cylinder mean temperature – Case 1

When observing the mean temperature inside the cylinder, it can be observed that the mechanism obtained slightly higher values for D100 compared to the experiment. Earlier ignition of D100 is also visible. The mechanism also predicts higher post-combustion temperatures than the experimentally obtained values. For the B20 blends, as per pressure behaviour, no significant difference is observed between the blends. The shortest ignition delay time of the tomato-seed mixture is also visible in the temperature curvatures. Overall, the combustion process is shorter with lower peak temperatures. Also, significantly lower temperature values after the combustion are observed.
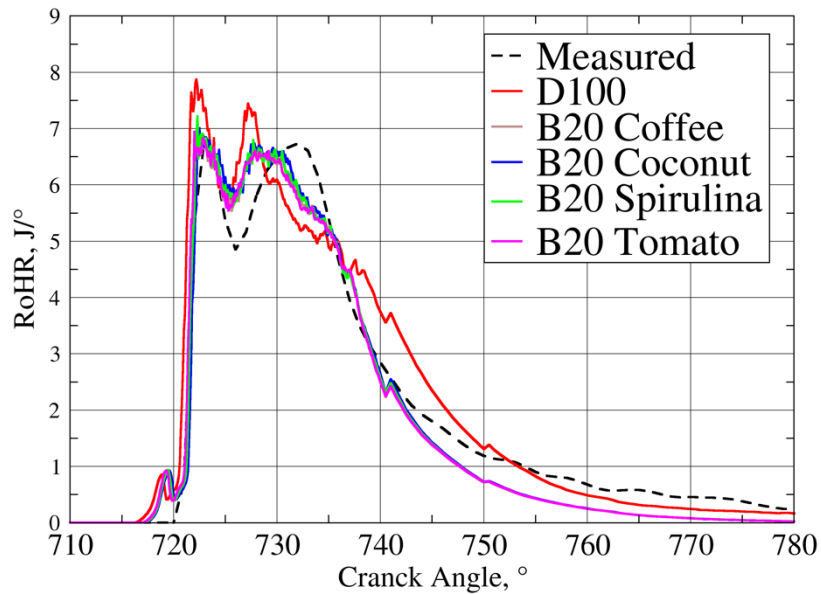
Figure 12　Rate of Heat Release for B20 blends – Case 1

In Figure 12, the RoHR shows a good correlation to the pressure inside the cylinder. The values for D100 show rapid ignition at the beginning of the combustion, which corresponds to higher pressure values. Although biodiesel blends are very similar, the highest differences are between coconut oil and tomato-seed oils, with Spirulina and WCGO overlapping. Ignition delay times are in agreement with the pressure curvatures in Figure 10, as the tomato-seed oil blend has the shortest ignition delay, followed by the Spirulina and WCGO mixtures and coconut oil igniting the latest. Also, a high drop in pressure during the expansion cycle is visible due the lower release of energy for all the biodiesel blends.
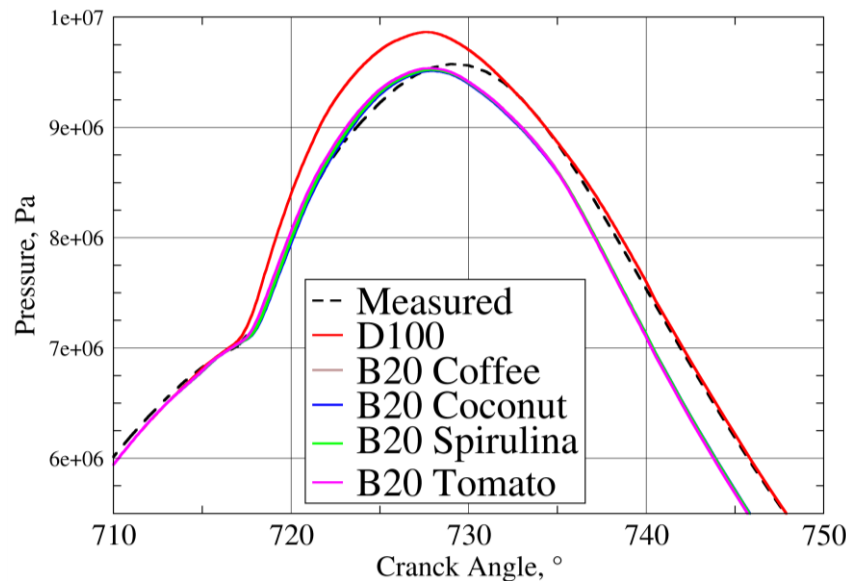
Figure 13 In-cylinder pressure distribution of B20 blends – Case 2

Similarly, as shown in Case 1, Case 2 showed an increase in peak pressure for the modelled D100 diesel compared to experimental values. Also, the ignition delay time was slightly shorter, but the combustion process seems to be more intensive as the pressure gradient of the modelled diesel is significantly higher. When comparing the in-cylinder pressure of the biodiesel blends to D100, a reduction in peak pressure of 3 % is obtained. Compared to Case 1, this smaller difference in peak pressure can be due to a stronger swirling motion (Table 6), leading to better dispersion of the fuel particles injected into the combustion chamber and resulting in better combustion. Looking at the feedstock, all three blends behave the same, meaning that under higher swirl motion, the chemical structure does not have a high impact on the combustion performance of biodiesel.
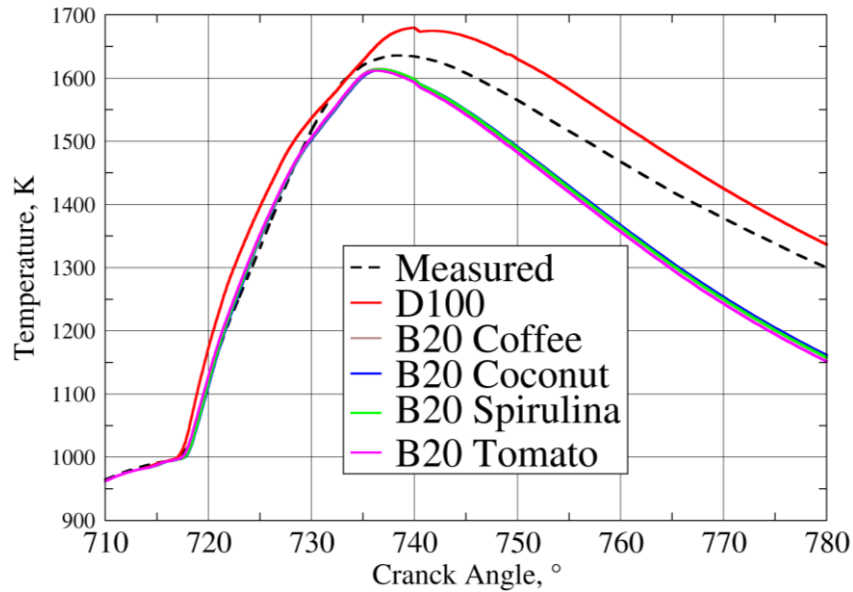
Figure 14 In-cylinder mean temperature – Case 2

Corresponding to the pressure values, the mean in-cylinder temperatures are higher for D100 during the entire expansion stroke. Moreover, compared to Case 1, the temperatures are higher for all the B20 mixtures. Again, this behaviour is due to higher swirling motion allowing the flame front to expand much more into the combustion chamber and enhance the heat transfer via convection.
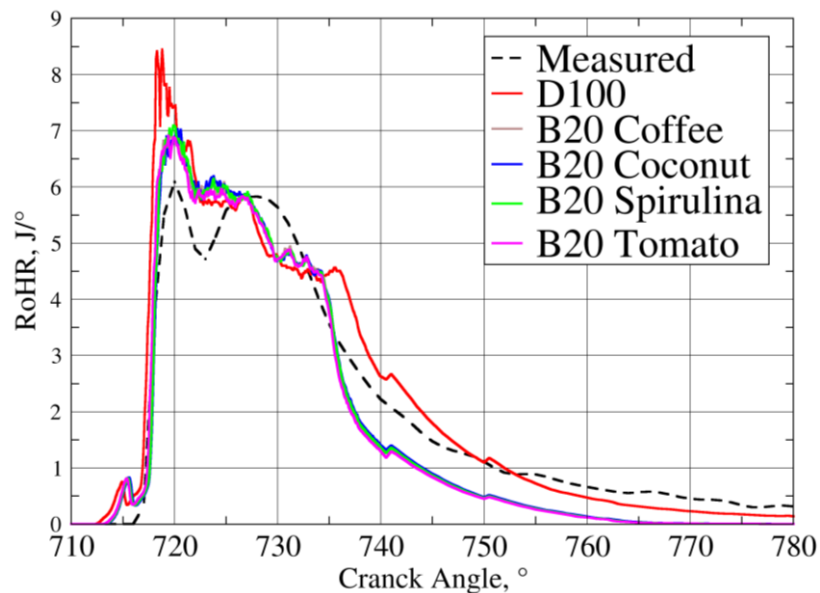

Figure 15 Rate of Heat Release for B20 blends – Case 2

The fast and intensive ignition in Figure 15 corresponds to bigger pressure gradients of Case 2. The difference in biodiesel blends concerning the released heat is negligible, which is in accordance with pressure behaviour.
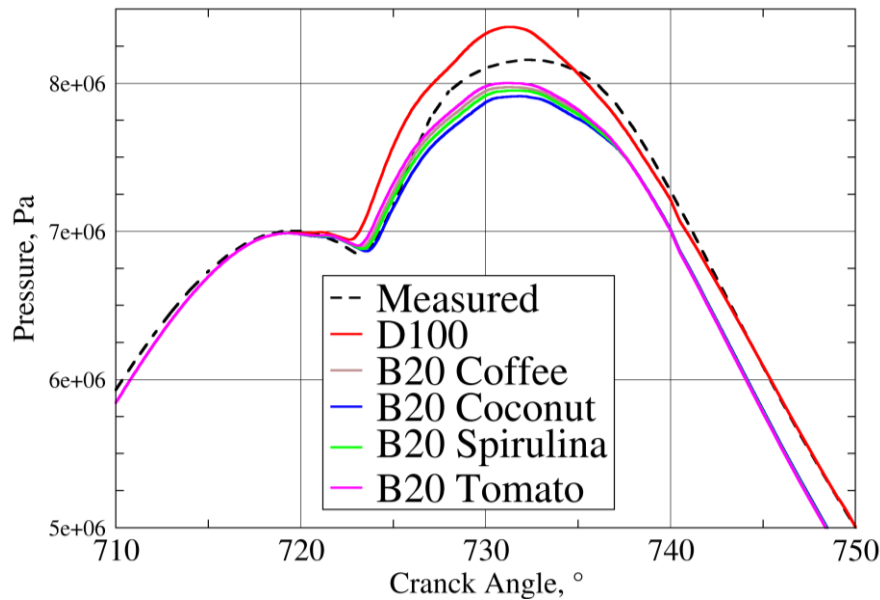

Figure 16 In-cylinder pressure distribution of B20 blends – Case 3

Case 3 is specific for its longer ignition delay times. As for all cases, the n-heptane surrogate in D100 tends to ignite sooner than the experimentally obtained values. Comparing the biodiesel blends to the D100, a reduction of 6 % in peak pressure was obtained, with the highest pressure being in the tomato-seed blend. As in Case 1, the influence of the chemical structure is the same. The blends with a higher share of unsaturated FAME ignite sooner and have a slightly higher peak pressure than those with a higher share of saturated FAME. Along with the influence of the chemical structure, Case 3 is specific for its lowest pressure inside the cylinder prior to ignition, which also entails lower temperatures automatically resulting in even longer ignition delay times visible in Figure 16. The swirling motion values are not as high as in Case 2, therefore, combined with overall lower in-cylinder temperature values, less intensive combustion occurred.
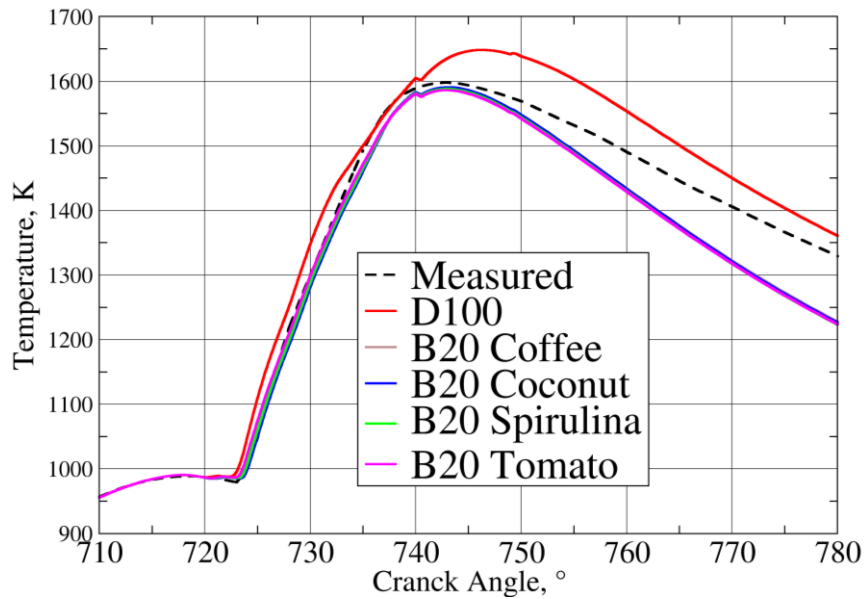
**Figure 17 In-cylinder mean temperature – Case 3**

Following the behaviour of the previous cases, the temperature curves are similar for all biodiesel blends. The longer ignition delay time is more pronounced, but there are no significant differences among the biodiesel mixtures.
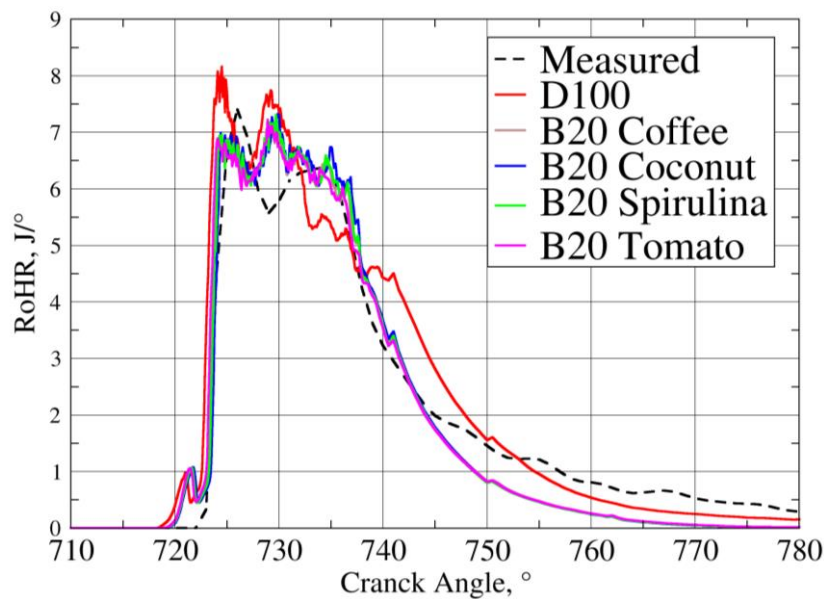
Figure 18 Rate of Heat Release for B20 blends – Case 3

Similar to Case 1, in Figure 18, D100 shows rapid ignition and higher peak values compared to the experimental values. Looking at the B20 blends, it can be seen that the highest RoHR values are obtained around 730 CA°. This behaviour is probably due to a much longer ignition delay

compared to other cases. Also, looking at the released energy during the expansion cycle, a higher drop in the released energy is observed in all cases. Due to overall lower amounts of released energy, a lower pressure during the expansion cycle is observed for all biodiesel blends.
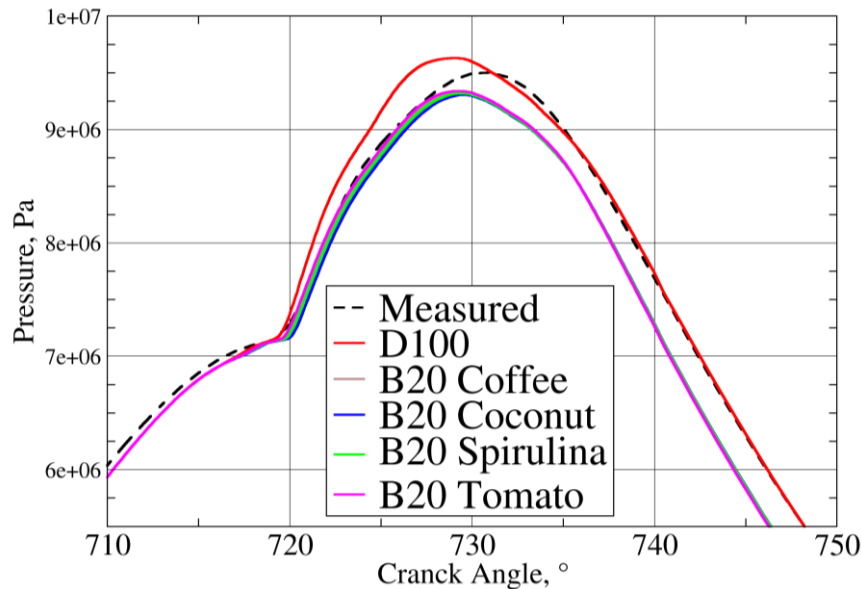
**Figure 19 In-cylinder pressure distribution of B20 blends – Case 4**

D100 again showed a much higher pressure gradient for the fourth operating point, but its peak value was much closer to the measured data. B20 blends showed a reduction in peak pressure of approximately 3.5 %, proving that the higher swirling motion Cases show better combustion performances. Comparing the initial conditions of Case 4 and Case 2 (Table 6), both cases had high initial pressure and swirl values. However, due to the slightly higher pressure values of Case 2, a bigger pressure gradient and shorter ignition delay times were observed.

The chemical structure shows little to no influence concerning the combustion performances in high swirl conditions.
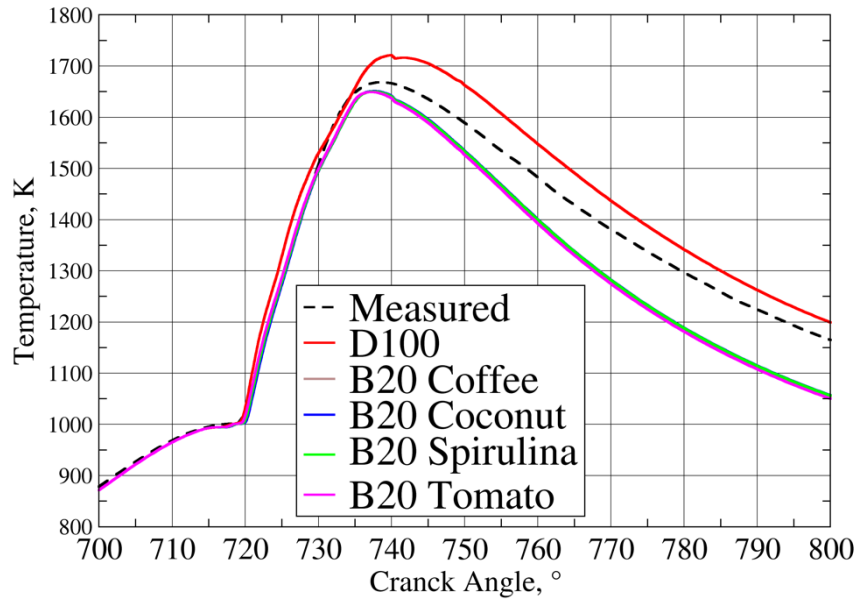
Figure 20 In-cylinder mean temperature – Case 4

Similarly to Case 2, due to higher swirling motion, the ignition delay times for all mixtures are practically the same. The D100 fuel still shows a slightly higher temperature gradient and overpredicted peak values than the measured values.
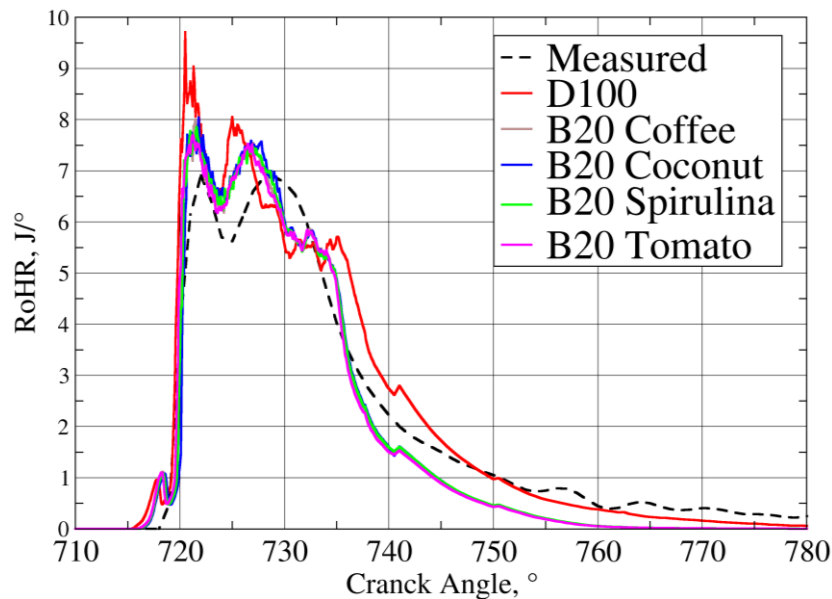

Figure 21 Rate of Heat Release B20 blends – Case 4

In Figure 21, D100 shows an overpredicted peak value during ignition, which correlates to the overpredicted pressure gradient in Figure 19. Meanwhile, all the blends show similar behaviour throughout the combustion process. When compared to Case 2, higher peak values are

observed. This behaviour is due to higher initial oxygen content in Case 4, resulting in a more profound combustion.

4.2   B50 Blends

When mixed in 50 % volumetric share, the chemical structure has a more significant influence on the combustion characteristics in all the operating conditions.
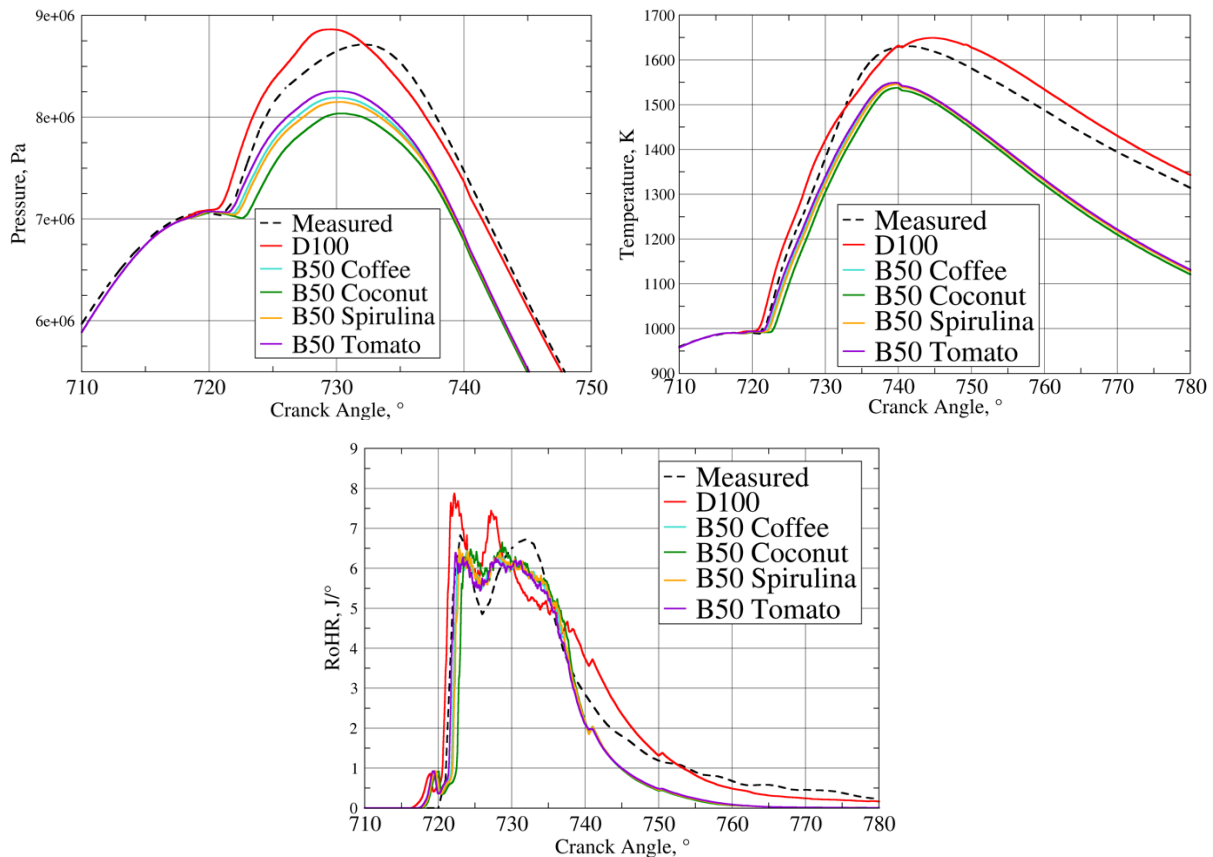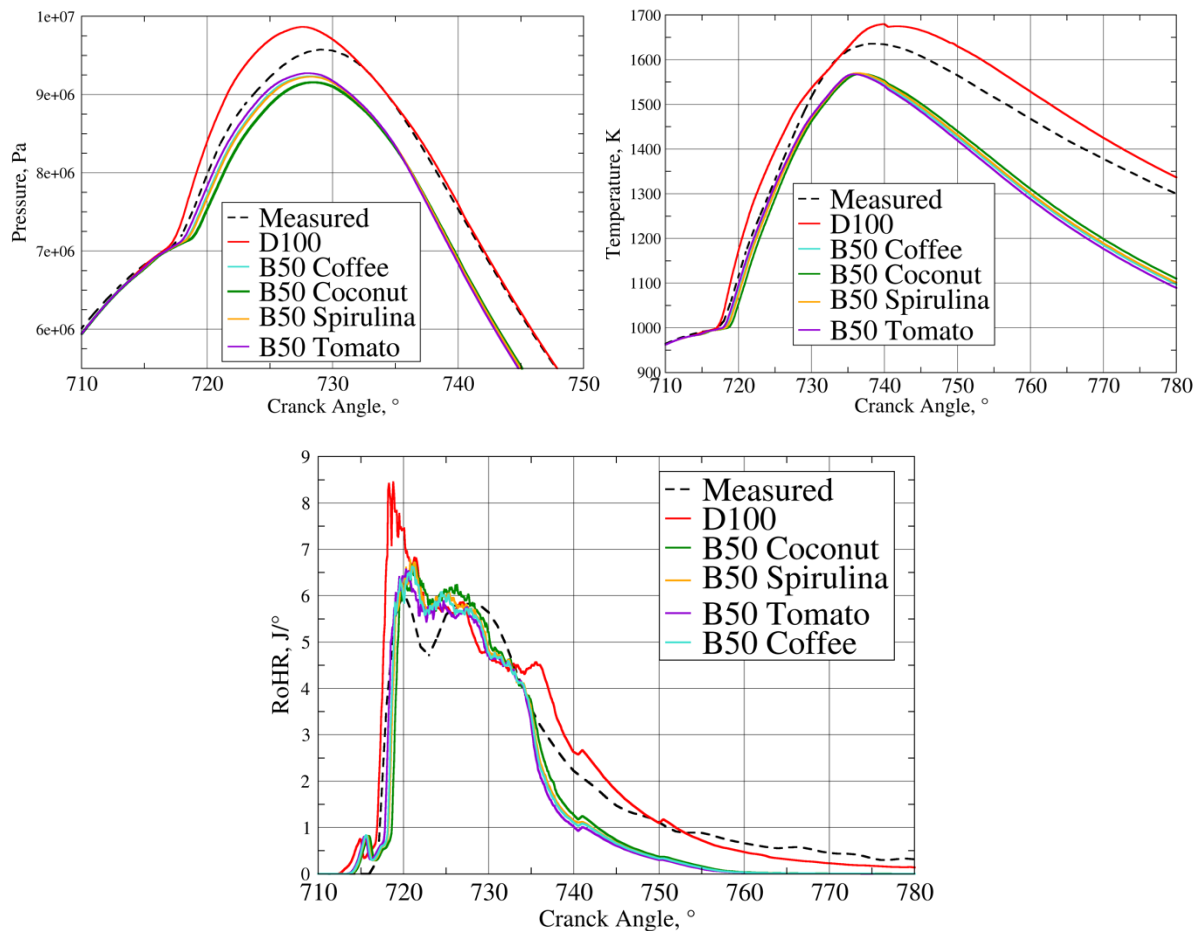

Figure 22 In-cylinder pressure, temperature and RoHR of B50 blends – Case 1

Figure 22 shows that all biodiesel blends tend to ignite later than the B20 blends, the coconut oil blend being the latest. Increasing the volumetric share of biodiesel in diesel, the chemical structure tends to have a higher impact on the combustion process. The higher difference is due to an even higher content of unsaturated methyl esters that contain a higher oxygen share than the shorter chained saturated methyl esters. This difference is best shown in the 3 % higher peak pressure of the B50 tomato compared to the B50 coconut blend. The longer ignition delay time is also visible in the temperature graph. The RoHR shows that the B50 blends have a much lower peak value than D100, and the ignition delay time is much more expressed than the B20

blends. Also, a significant drop in the released energy is observed when looking at the expansion cycle, corresponding to much lower pressure and temperature values.

Figure 23 In-cylinder pressure, temperature and RoHR of B50 blends – Case 2

Following the trend of all operating points, the Coconut blend with the highest share of saturated FAME ignited last and produced the lowest pressure values as opposed to the highly unsaturated Tomato-seed mixture. Unlike the B20 mixture (Figure 13), the difference in ignition delay time is much more expressed.
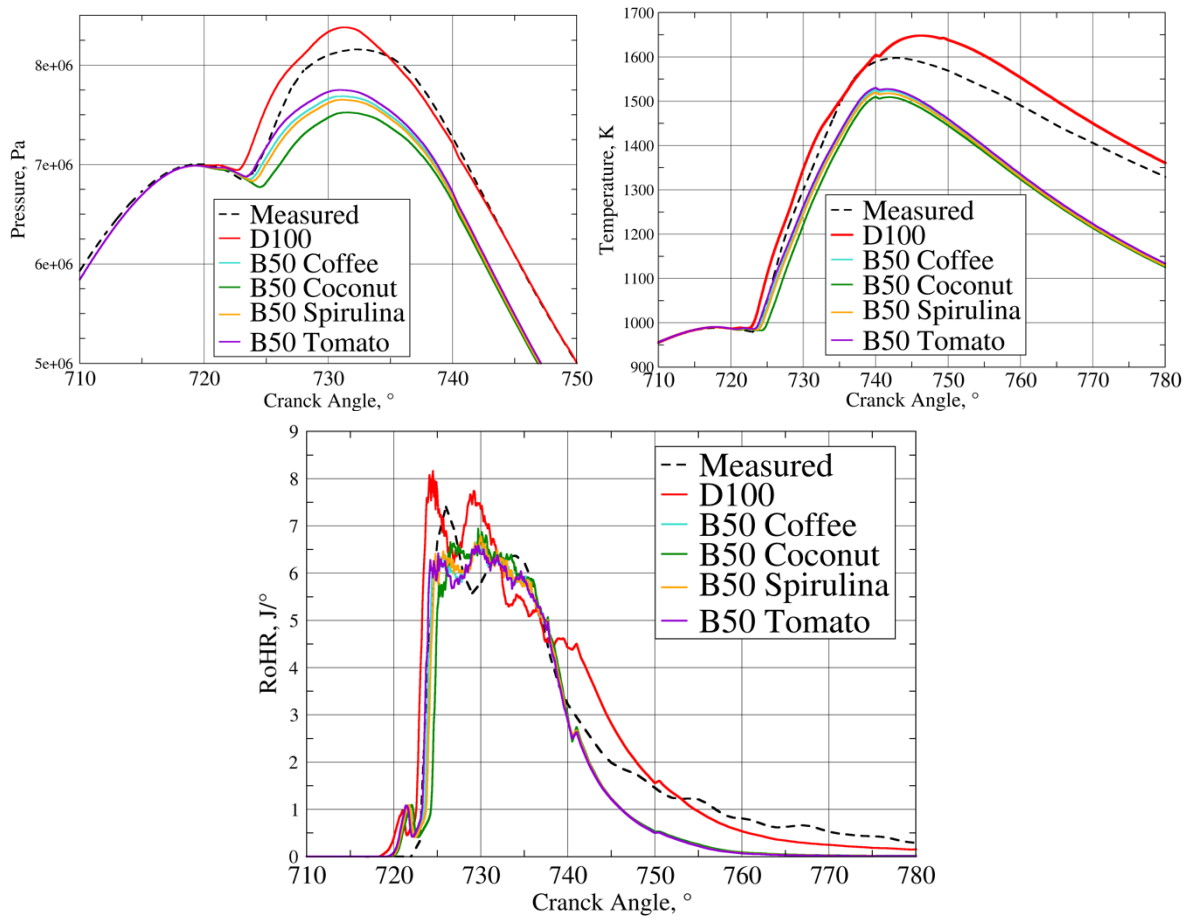
Figure 24 In-cylinder pressure, temperature and RoHR of B50 blends – Case 3

The behaviour of Case 3 operating point is similar for both B20 and B50 mixtures, as the very late time of ignition produces higher peak values later in the combustion process. The peak temperature values for the B50 blends are different from Case 1 and Case 2. Longer ignition delay time for Coconut blends significantly lowered the peak pressure and the overall released energy. The lower values of the released energy and the fast drop during the expansion cycle result in considerably lower pressure and temperature values inside the cylinder. Concerning the influence of the chemical structure, a 3 % difference in peak pressure between the tomato and coconut feedstock is observed.
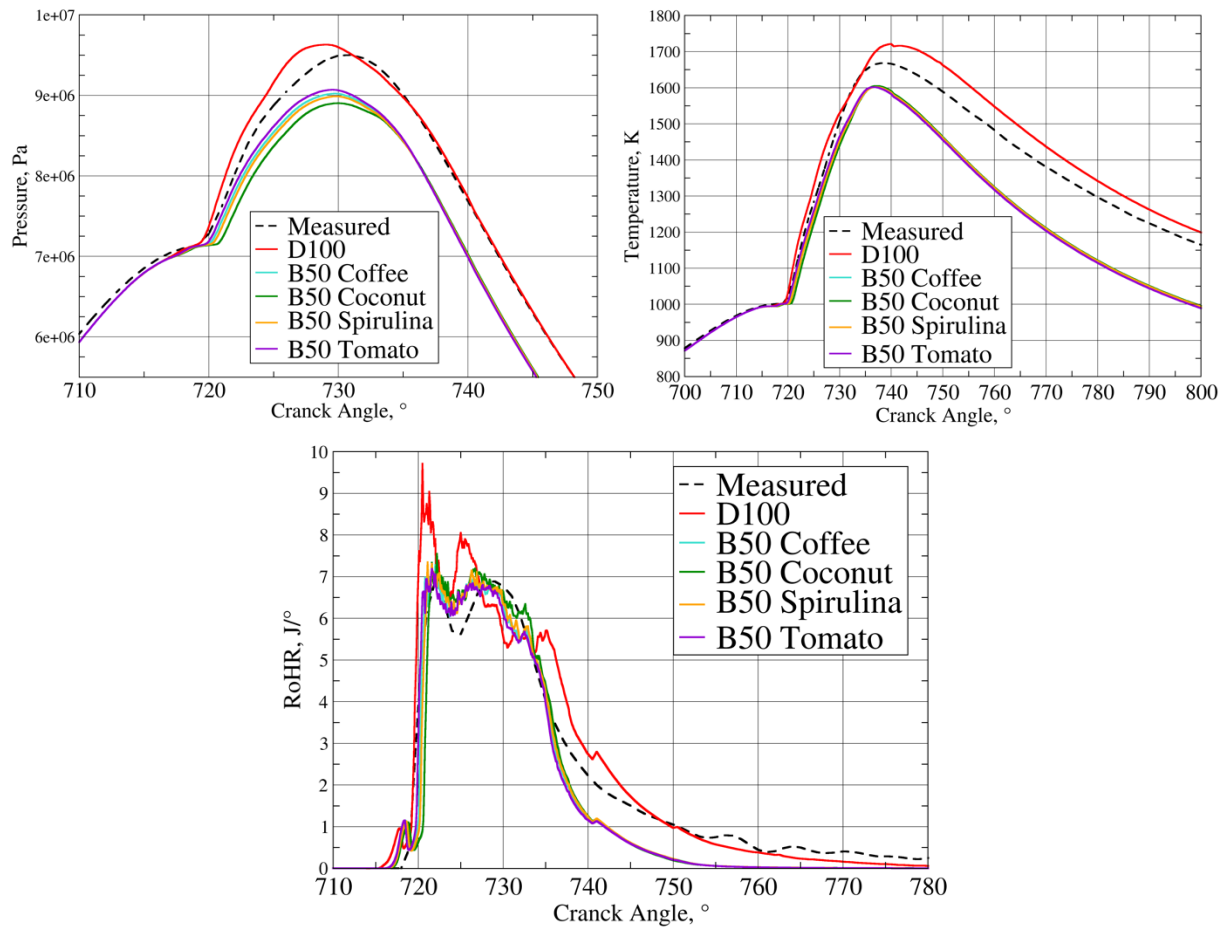
Figure 25 In-cylinder pressure, temperature and RoHR of B50 blends – Case 4

Comparing the peak pressure values of B50 mixtures to D100, an 8.5 % reduction was observed. In all the analyzed cases, all biodiesel blends showed lower peak pressure and lower released energy than conventional diesel. Released energy can be obtained by calculating the surface under the RoHR graph. A Lower Heating Value (LHV) of conventional diesel fuel is around 43 MJ/kg. Due to its higher oxygen content, Biodiesel has a lower carbon and hydrogen contents, lowering its mass energy content by about 10 %, depending on the feedstock [34]. By analysing LHV for D100 and Coconut feedstock blends in Case 3, lower values for biodiesel blends were obtained.

Table 15   LHV values for D100 and Coconut oil mixtures – Case 3

	Measured	**D100**	**B20 Coconut**	**B50 Coconut**
LHV [MJ/kg]	43.3	45.3	37.8	32.3

Due to its lower mass energy values, by increasing the share of biodiesel in the diesel-biodiesel blends, the energy content decreases. This trend is visible in Table 15. However, the computed values are somewhat lower compared to the literature. The usage of surrogate species can justify this behaviour as the mass fraction of oxygen decreases by increasing the carbon chain of fatty acids, the heating value increases [38]. Due to these actions, short-chained surrogates MD ($C_{11}H_{22}O_2$) and MD9D ($C_{11}H_{20}O_2$) exploit lower heating values. Moreover, as the cylinder pressure is dependent on the fraction of fuel burning in the premixed phase and its ability to mix well with the air in the combustion chamber, Biodiesels' high viscosity and low volatility lead to poor atomization and poor mixture with air lowering the pressure values [39].

4.3 Injected mass adaptation

Due to lower values of LHV for biodiesel blends, a smaller amount of energy was released per the same amount of injected fuel. Therefore, an analysis was performed to check whether the combustion characteristics of the experimental fuel can be matched with a diesel-biodiesel mixture by altering its injected fuel.

By calculating the surface under the RoHR curve, the released energy can be obtained. The analysis was performed for Case 3 and both coconut oil mixtures, including the n-heptane surrogate (D100). The calculated released energy for 1/8 of a cylinder is $Q_{EXP} = 147.03$ J. By dividing the released energy by an LHV value, a new corrected mass can be obtained. For D100:

$$m_{D100_{corr}} = \frac{Q_{EXP}}{LHV_{D100}} = \frac{147.03 J}{45300000 \, J/kg} = 3.25 \cdot 10^{-6} \, [kg] \tag{29}$$

A 4 % reduction in injected mass for D100 is observed.

For B20 coconut blend:

$$m_{B20_{corr}} = \frac{Q_{EXP}}{LHV_{B20}} = \frac{147.03 J}{37800000 \, J/kg} = 3.89 \cdot 10^{-6} \, [kg] \tag{30}$$

Compared to the initial mass, an 14.6 % increase in the injected fuel mass was gained.

And for the B50 coconut blend:

$$m_{B50_{corr}} = \frac{Q_{EXP}}{LHV_{B50}} = \frac{147.03 J}{32300000 \, J/kg} = 4.55 \cdot 10^{-6} \, [kg] \tag{31}$$

A 34% increase in the injected fuel mass was gained.

Figure 26 shows the obtained values for the B20 coconut oil blend with a higher amount of fuel injected. It can be seen that the combustion process improved significantly. The combustion process is more intensive than the experimental fuel, with higher peak values in all the characteristics. The ignition delay time is the same as the experimental values, but when ignition

occurs, it is more rapid, as seen from the slightly higher pressure and temperature gradients. Also, a higher pressure during the expansion cycle corresponds to higher amounts of released energy. An 8 % increase in peak pressure values was obtained compared to the B20 values with lower mass injected. For the D100 case, due to the reduction in injected fuel, a decrease in overall performance is noted. Slightly lower pressure values are observed due to lower amounts of released energy.
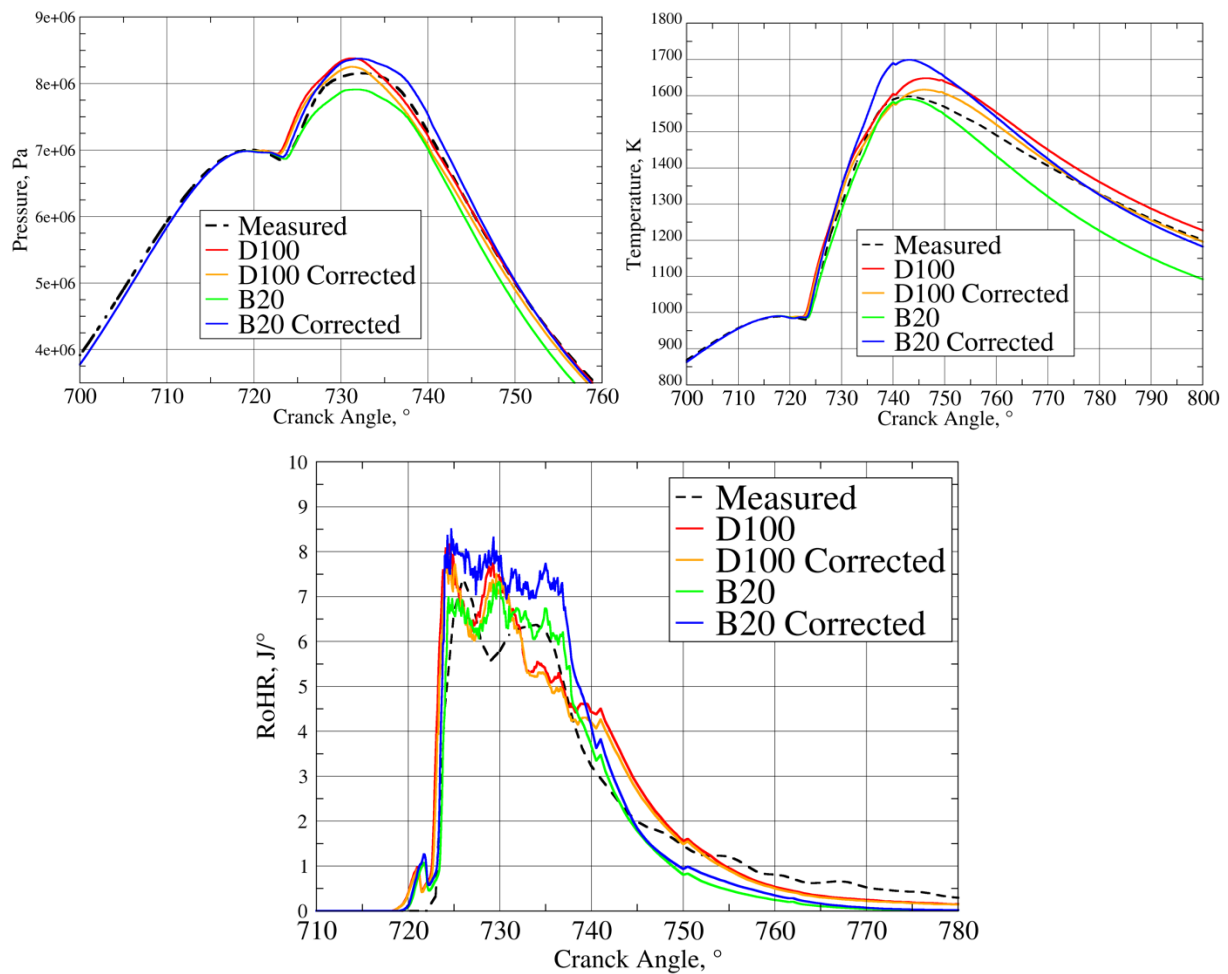
Figure 26 In-cylinder pressure, temperature and RoHR for B20 blends with corrected injected mass – Case 3

For the B50 blend, similar behaviour is observed in Figure 27. Again, overall better combustion is obtained, as higher pressure and RoHR peak values are observed. A significant increase in the peak value of RoHR is subject to higher amounts of biodiesel being injected into the combustion chamber. For this reason, with higher amounts of oxygen inside the fuel, more profound combustion can be obtained inside the cylinder. For the B50 Coconut mixture, an 16 % increase in peak pressure was obtained by increasing the fuel injected mass into the cylinder.
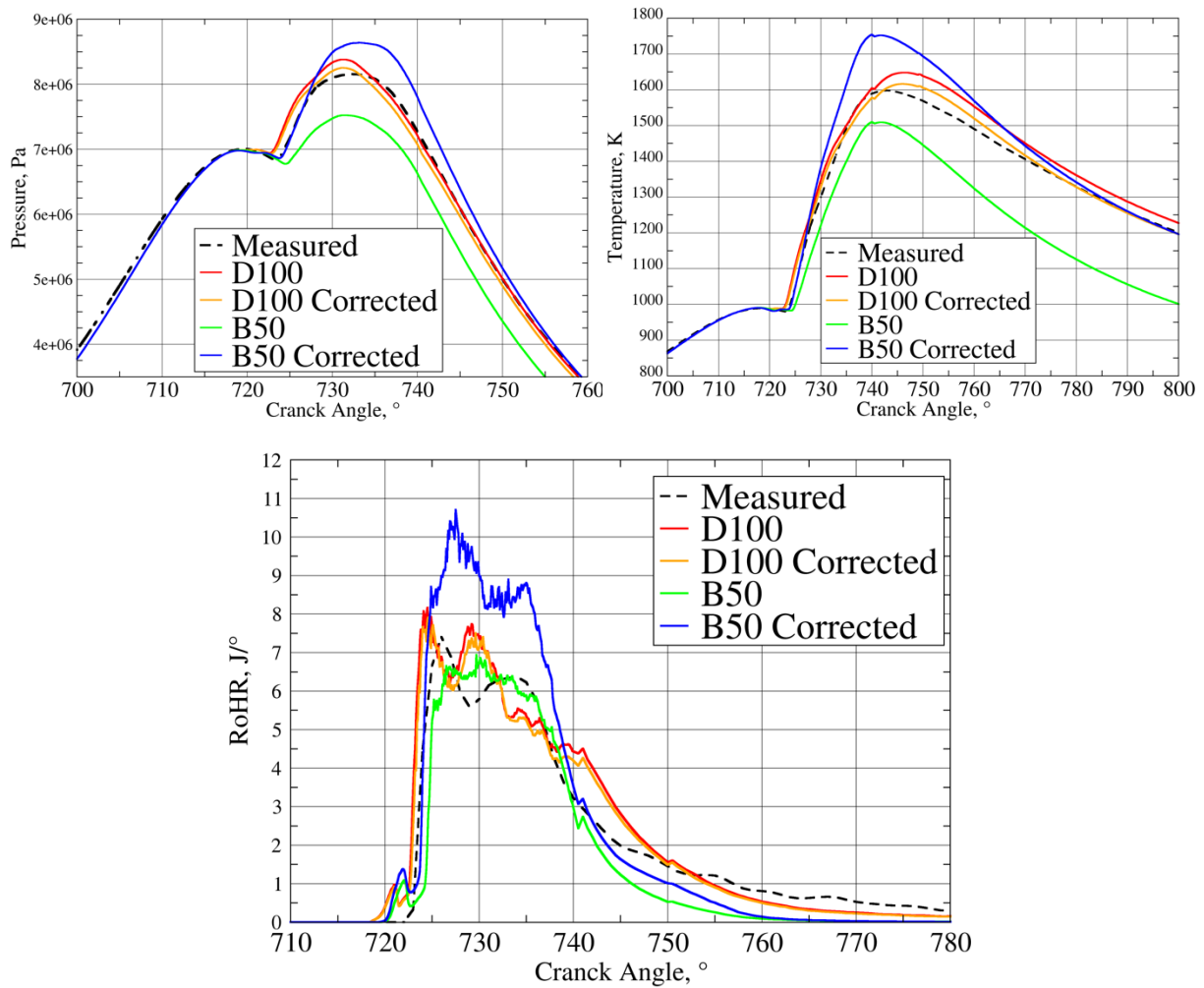
Figure 27 In-cylinder pressure, temperature and RoHR for B50 blends with corrected injected mass – Case 3

Due to biodiesel's lower mass energy, more fuel needs to be injected into the combustion chamber to match the combustion characteristics of conventional diesel. Depending on the volumetric content of biodiesel in the fuel blend, up to a 34 % increase in the injected fuel mass needs to be performed. For this case, both coconut blends showed good agreement during the compression and the expansion cycle. However, slightly higher-pressure values were obtained during the ignition process, which can be adjusted by altering the specific simulation parameters.

4.4 Temperature distribution

The following chapter will look at the temperature field of a single operating point. Side-to-side comparison of temperature fields for all generation feedstocks in the B20 share will be analyzed first. Then a single feedstock will be compared in B20 and B50 share respectfully. WCGO blends were not observed as their behaviour is the same as of the Spirulina blend.
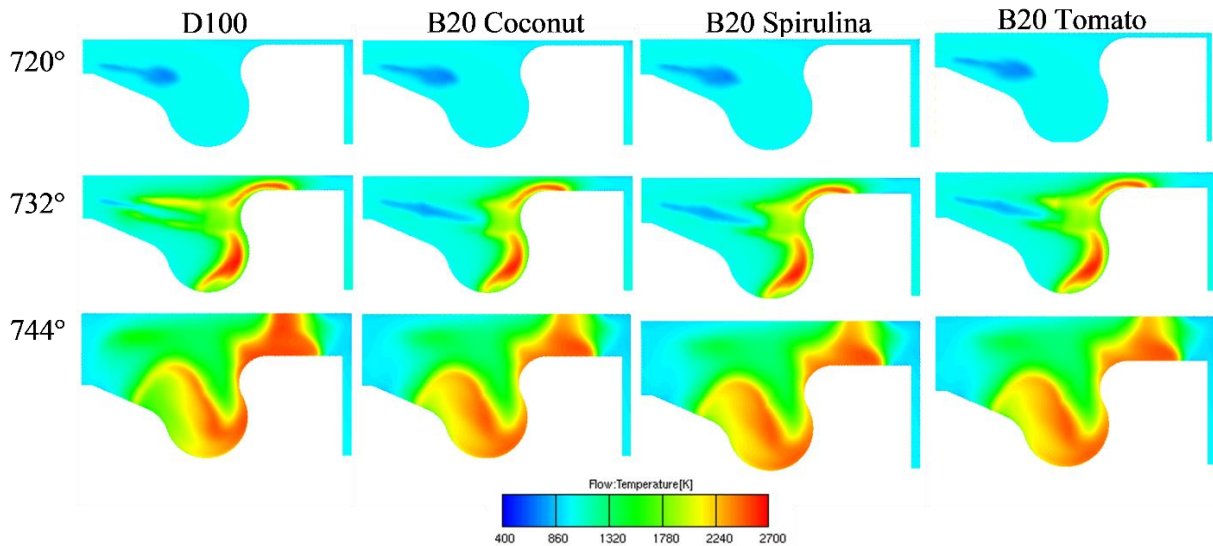
**Figure 28   Temperature field for B20 blends - Case 3**

The temperature field for Case 3 is shown. When the fuel is injected into the pressurised gas mixture, it is injected at a lower temperature than the gas inside the combustion chamber. Since the fuel is injected in liquid form, the energy necessary for the latent heat of vaporization is transferred from the internal energy of the gasses inside the cylinder. Therefore, the cooling of the gas phase is visible at around 720 CA°. Due to higher temperature conditions, the evaporated fuel ignites, and the combustion process commences at the periphery of the spray vapour cloud as seen at around 732 CA°. A significant difference is visible around the spray vapour as the flame starts to consume the evaporated fuel. It can be noticed that for the D100 fuel, at 732 CA°, almost all the fuel ignited, whereas, for the B20 blends, a significant share of the injected fuel is still not ignited. When only looking at the B20 blends, it can be seen that the combustion process in the tomato-seed mixture diffused much further toward the injection point than in the coconut oil mixture. This behaviour corresponds to Figure 16, where we can see a shorter ignition delay time for tomato-seed oil. Later, at around 744 CA°, due to turbulent behaviour inside the combustion chamber, the fuel vapour diffuses away from the spray axis and moves towards the compensational volume where the highest temperatures are found.
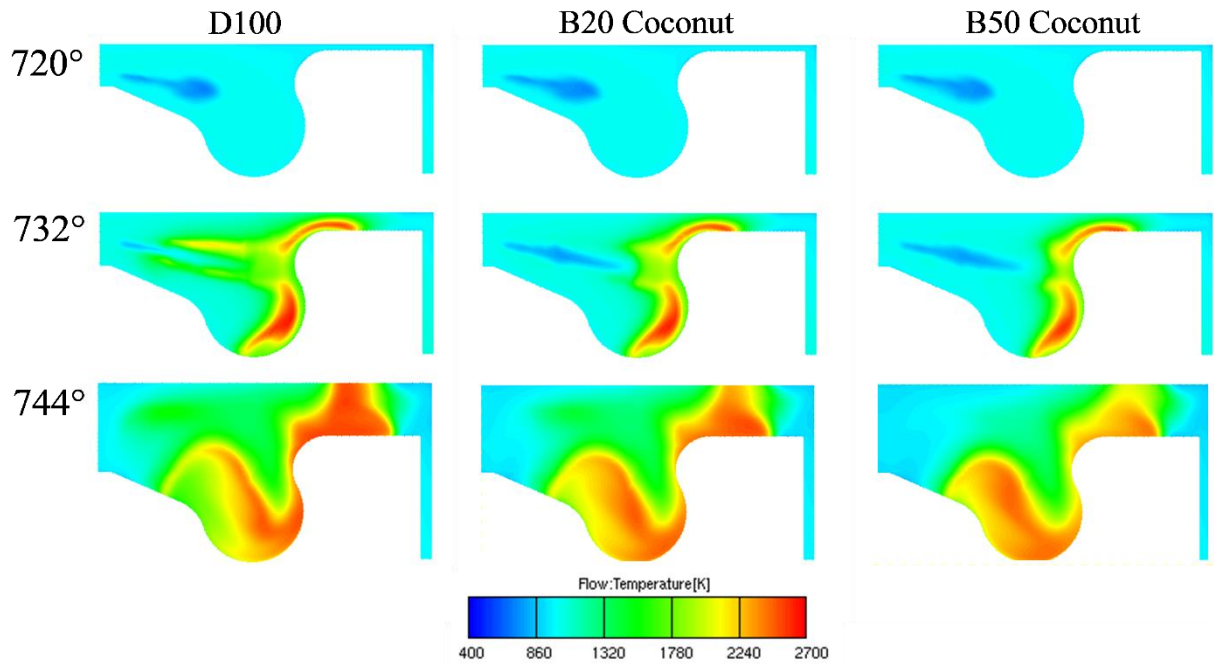
Figure 29 Temperature field for Coconut oil blends - Case 3

Figure 29 shows the temperature field for B20 and B50 blends of coconut oil. There are visible differences in the two blends, as the temperature field is much lower for the B50 blend showing good agreement with the pressure and RoHR values analyzed previously. Around 720 CA°, no noticeable differences are seen. However, at 732 CA°, less fuel is ignited in the higher volume mixture. Later in the combustion process, much lower peak temperature areas are observed.
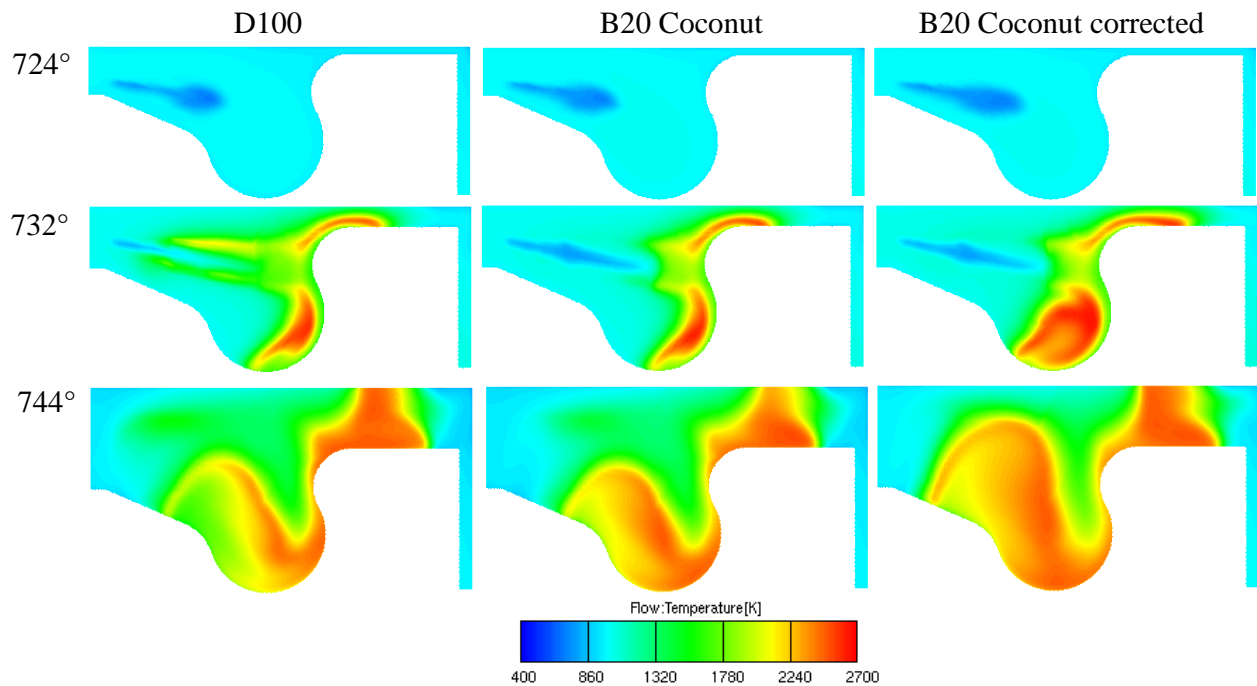
**Figure 30 Temperature comparison for a different amount of injected B20 Coconut oil fuel -
Case 3**

Figure 30 shows the temperature field for the corrected amount of injected fuel. Significant differences are observed. During injection, a bigger cloud of lower temperature is formed, suggesting a higher amount of fuel being injected inside the cylinder. As seen in Figure 26, more intense combustion occurs with higher temperature values. Generally, more uniform combustion occurs throughout the cylinder when there is a more efficient mixing of fuel and air involved.
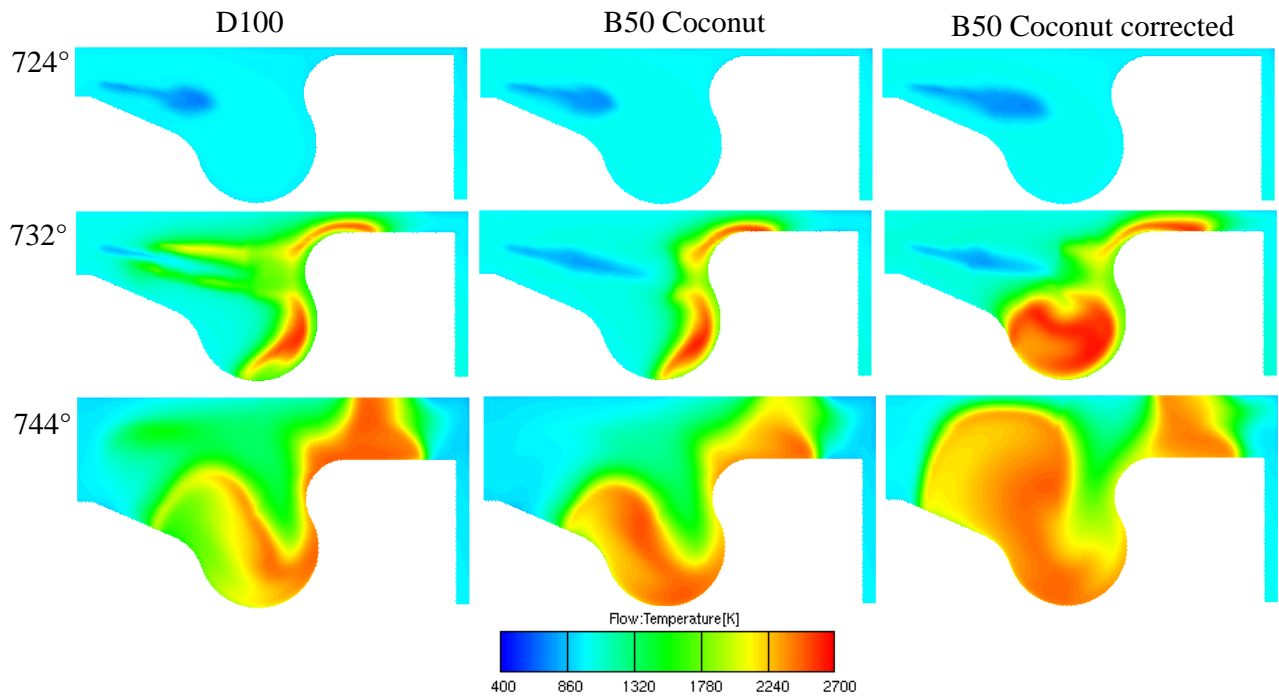
Figure 31 Temperature comparison for a different amount of injected B50 Coconut oil fuel - Case 3

The B50 Coconut oil blend with the higher amount of injected fuel behaves similarly to the B20 blend. A larger amount of injected fuel results in an even bigger cloud of lower temperature. When combustion begins, higher temperatures are formed around inside the piston bowl, and during expansion, a more uniform temperature field is formed compared to D100, and B50 blend with lower amounts of fuel injected

4.5 NO_x emissions results

NO_x pollutants are formed under high-temperature conditions around the flame region, with higher temperatures and higher flame propagation rates. Compression ignition engines highly contribute to NO_x emissions due to higher temperatures achieved inside the combustion chamber compared to other types of ICE. During diesel combustion, NO_x pollutants are predominantly formed in the shape of nitrogen oxide (NO). Considering this, the influence of the other NO_x compounds has been neglected in this thesis. The mass fraction of NO formed in all operating points under different conditions is shown in Table 16.

Table 16　NO mass fraction in exhaust gases (ppm)

|	**Measured**	**D100**	**B20 Coconut**	**B50 Coconut**	**B20 Spirulina**	**B50 Spirulina**	**B20 Tomato**	**B50 Tomato**
Case 1	562	407	290	172	298	200	303	224
Case 2	592	497	378	263	384	281	389	294
Case 3	368	262	172	77	177	100	186	120
Case 4	859	663	515	367	523	390	534	414

Looking at the formed NO, it can be seen that the kinetic mechanism underpredicted NO formation in all the cases for pure diesel (D100). The highest difference of 38 % can be observed for Case 1. For the biodiesel blends, the NO formation directly correlates with temperatures, as the higher the temperatures more NO is formed. For Case 3, all the blends emitted the lowest amounts of NO as the peak temperatures were the lowest of all observed cases. On the other hand, Case 4, which showed the most effective combustion of the observed cases, also showed that the highest amounts of NO were formed.
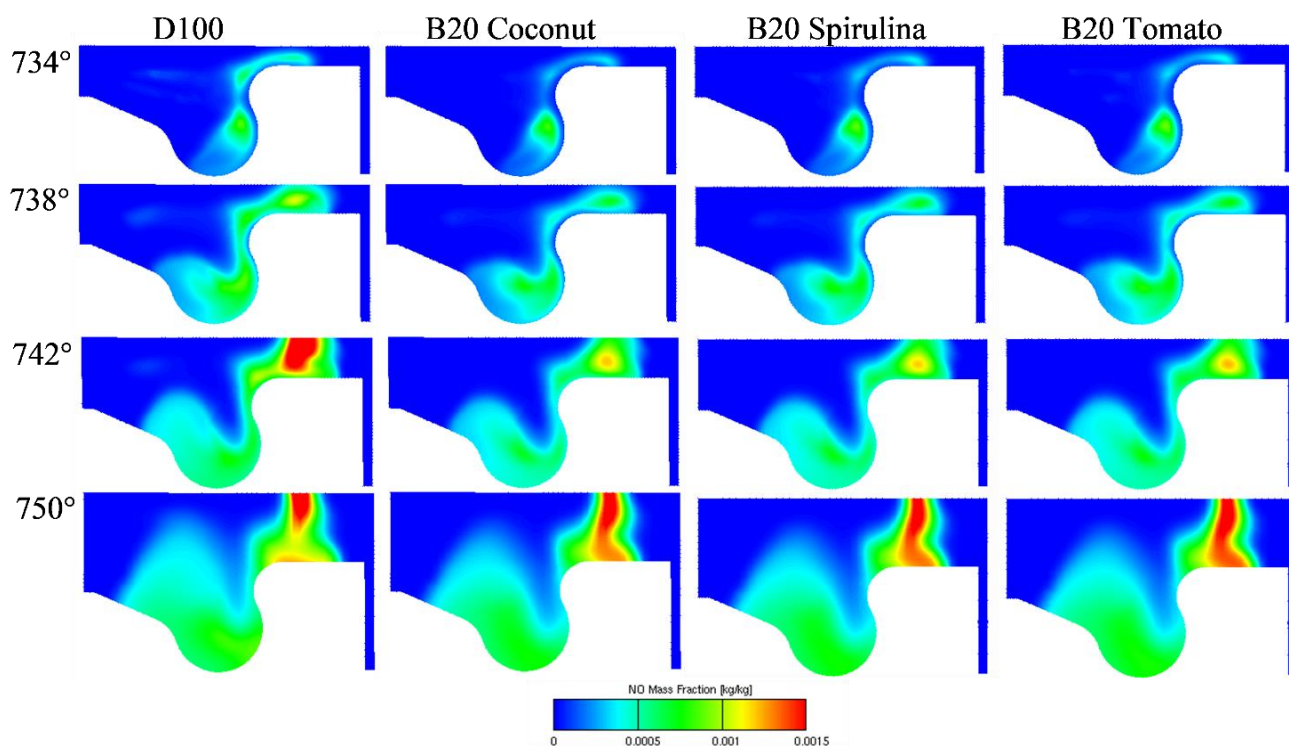
Figure 32　NO mass fraction for B20 blends – Case 3

Comparing the NO formation inside the cylinder by the feedstock type, many similarities are observed. Looking at Table 16, all the mixtures have similar NO content at the end of the cycle. The Tomato blend has the highest NO share, corresponding to slightly higher temperatures inside the cylinder during combustion. In Figure 32, all B20 blends are compared at the same

CA° times. The highest difference can be seen comparing the blends to D100 fuel, where combustion occurred much faster and at higher temperatures. At 742 CA°, D100 was at much higher temperatures which can be seen by a big cloud of NO forming near the cylinder head. This behaviour corresponds to temperature field inside the cylinder shown in Figure 28 where the highest temperatures are observed at the cylinder walls near the cylinder head. Between the different feedstocks, all blends showed the same behaviour during combustion. The following figure shows a comparison of the B20 and B50 blends of Coconut oil.
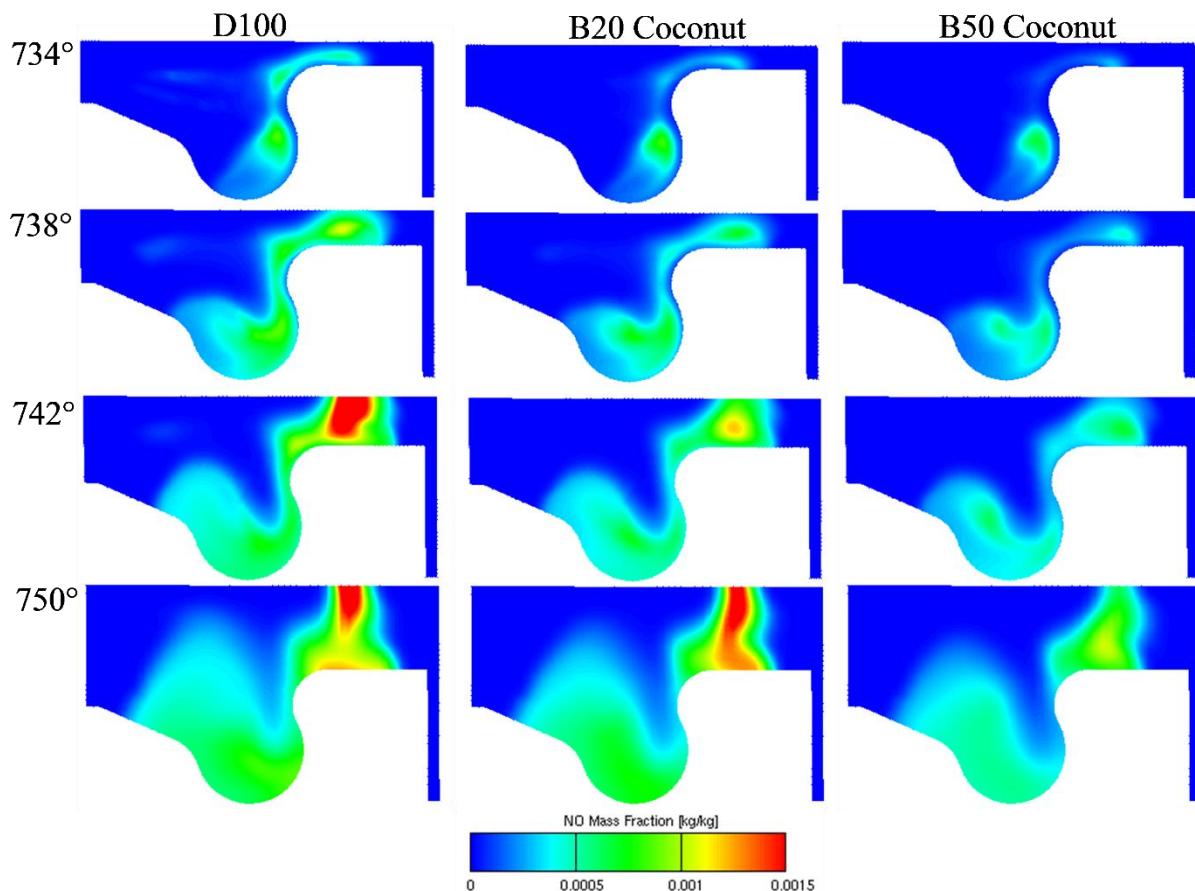
Figure 33 NO mass fraction for Coconut oil blends - Case 3

More significant differences can be observed when comparing the B20 to B50 blends. The combustion characteristics analyzed previously showed that fuels with higher Biodiesel share tend to ignite later and reach lower temperatures. This is also visible in the NO formation inside the cylinder. Due to lower temperatures, smaller amounts of NO are formed inside the cylinder.

Furthermore, NO emissions for the Coconut oil blends with the corrected mass injected were also analyzed. The amount of NO formed during one cycle is shown in Table 17.

Table 17   NO mass fraction from the corrected mass Coconut blends

|	**Measured**	**D100**	**D100 corrected**	**B20 Coconut**	**B20 Coconut corrected**	**B50 Coconut**	**B50 Coconut corrected**
Case 3	368	262	248	172	237	77	245

Higher amounts of NO are released by trying to obtain similar released energy as the experimental fuel. As shown in Figure 26 and Figure 27, higher temperatures were obtained in the cylinder for the coconut blends with the corrected mass. Due to these higher local temperatures, more NO is formed in the cylinder. Compared to D100 fuel with the corrected amount of injected fuel, a decrease in NO of 4.6 % and 1.2 % for B20 and B50 is observed. Figure 34 compares the B20 Coconut blend with different masses of injected fuel to D100. Overall, the highest share of NO is found on the outer edges of the cylinder wall, but due to intense combustion, NO is more uniformly dispersed inside the cylinder than D100 and B20 with less fuel injected.
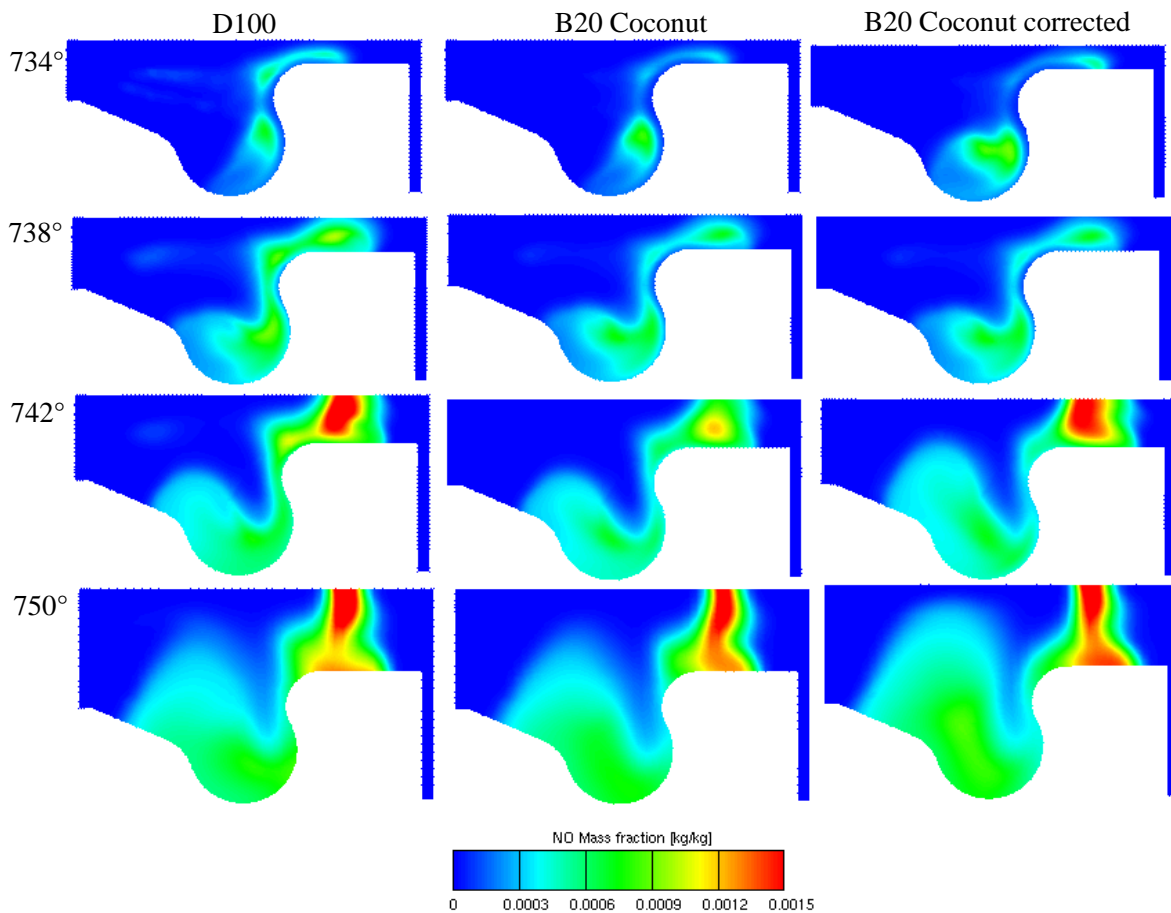
Figure 34 NO mass fraction comparison for a different amount of injected B20 Coconut oil fuel - Case 3

For the B50 coconut blend, the corrected mass showed the best combustion performance resulting in the highest pressure and temperature values. Due to such high temperatures (Figure 27), good oxidation of nitrogen led to a high share of NO inside the cylinder.
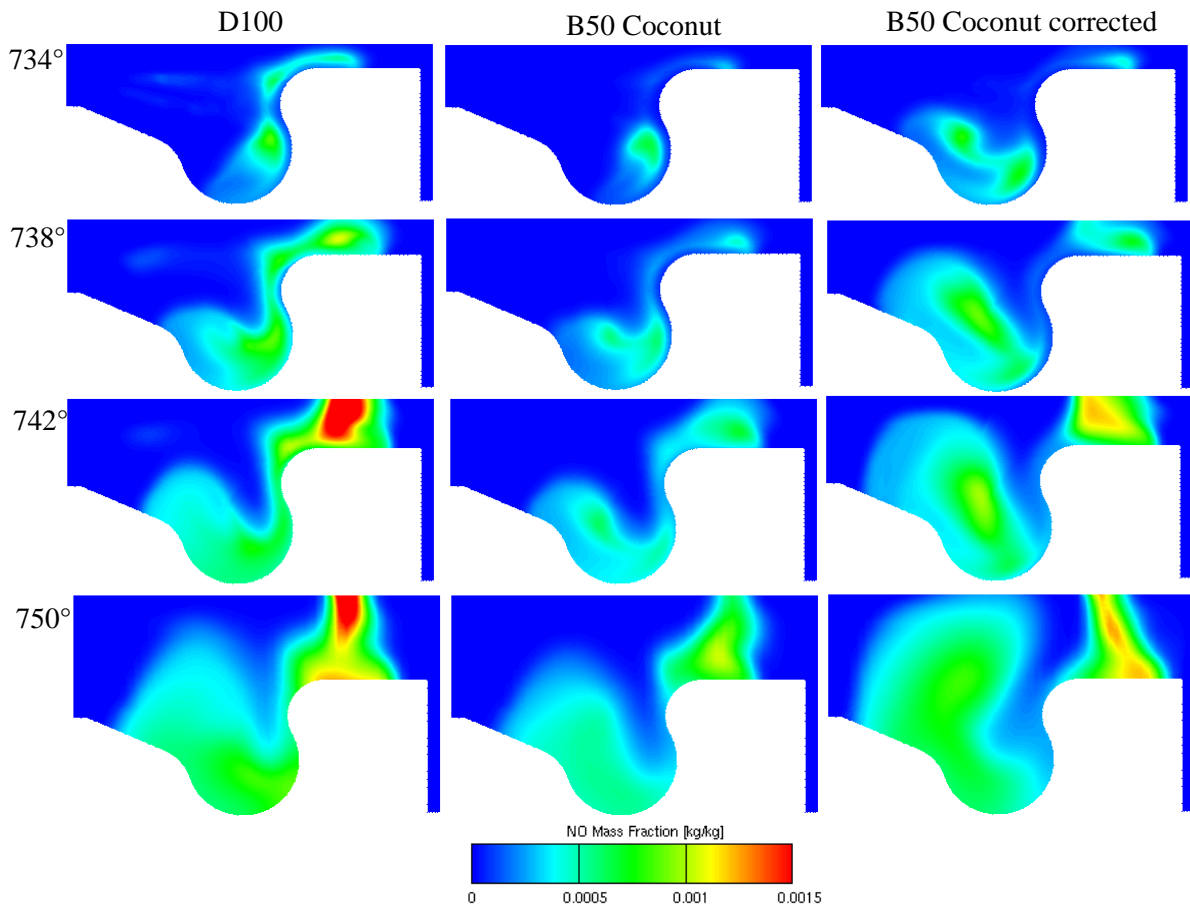
Figure 35 NO mass fraction comparison for a different amount of injected B50 Coconut oil fuel - Case 3

4.6 CO_2 emission

For the analysis of the emitted carbon dioxide, a simple case study was conducted to compare two different approaches for the CO_2 emission analysis. CO_2 emissions obtained via CFD simulations for one operating cycle were compared to yearly CO_2 emissions calculated via the CO_2 emission factor.

4.6.1   Comparison of CO_2 predictions between CFD simulation and emission factors

For the yearly emissions analysis of CO_2, the values of the average mileage and fuel consumption of a diesel-operated car in the European Union were taken from [40] Obtained values are:

- Yearly mileage of 19000 kilometres
- Fuel consumption of 6.4 l/100 km

By simple conversion, an amount of 1033.6 kg/year of diesel fuel is consumed per vehicle in the European Union.

The CO_2 emissions calculated by the Emission factors methodology are calculated with the following equation:

$$E_{CO_2} = A \cdot LHV \cdot EF_{fuel} \cdot OF$$

(31)

E_{CO_2} – CO_2 emissions $[t/year]$ (a ton of CO_2 per year)

A – the amount of consumed fuel $[kg/year]$, (kilogram of fuel per year)

LHV – lower heating value $[MJ/kg]$, (MJ per kilogram of fuel)

EF_{fuel} – emission factor of the specific fuel $[t/MJ]$ (a ton of CO_2 per MJ)

OF – oxidation factor

The fuels LHV are obtained from the analyzed biodiesel blends:

Table 18   LHV fuel values

Fuel	LHV [MJ/kg]
D100	45.29
B20 Coconut	37.83
B50 Coconut	32.34
B20 Tomato	37.71
B50 Tomato	32.95
B20 Coffee	37.91
B50 Coffee	32.84
B20 Spirulina	37.68
B50 Spirulina	32.60

The emission factor for diesel and biodiesel were acquired from the IPCC database:

Table 19   Emission factors for Diesel and Biodiesel

Fuel	EF [t CO_2/TJ]
Diesel	74.1
Biodiesel	76.8

By applying the Intergovernmental Panel on Climate Change (IPCC) guidelines, the value of the oxidation factor is 1, which implies that all the carbon inside the fuel is burnt. Finally, yearly CO_2 emissions for individual blends are obtained:

Table 20   Yearly emissions of CO_2 for analyzed blends

Fuel	E_{CO_2} [t/year]
D100	3.466
B20 Coconut	2.936
B50 Coconut	2.564
B20 Tomato	2.906
B50 Tomato	2.584
B20 Coffee	2.975
B50 Coffee	2.557
B20 Spirulina	2.925
B50 Spirulina	2.585

Results show an approximate 15 % reduction in CO_2 emissions when burning the same amount of B20 diesel-biodiesel fuels compared to plain diesel (D100). For the B50 blends, a 26 % reduction is achieved.

4.6.2   Simulated CO_2 emissions

With the CFD simulations, CO_2 emissions were analyzed after a complete operating cycle. This approach can obtain more precise values as direct amounts of hazardous gasses formed during combustion can be measured. CO_2 mass fractions at 860 CA° for Case 3 are shown in Table 21.

Table 21   Share of CO_2 in residual gases – Case 3

| Fuel	Mass fraction [kg/kg]
D100	0.1094
B20 Coconut	0.0970
B50 Coconut	0.0870
B20 Tomato	0.0970
B50 Tomato	0.0888
B20 Coffee	0.0973
B50 Coffee	0.0880
B20 Spirulina	0.0969
B50 Spirulina	0.0878

B20 blends showed a reduction of approximately 11 % in emitted CO_2 compared to conventional fuel, whereas B50 mixtures reduced CO_2 emission by 20 %.

A comparison between the two approaches was conducted. Figure 36 and Figure 37 show a relative comparison of diesel-biodiesel blends to conventional fuel (D100) for both methods.
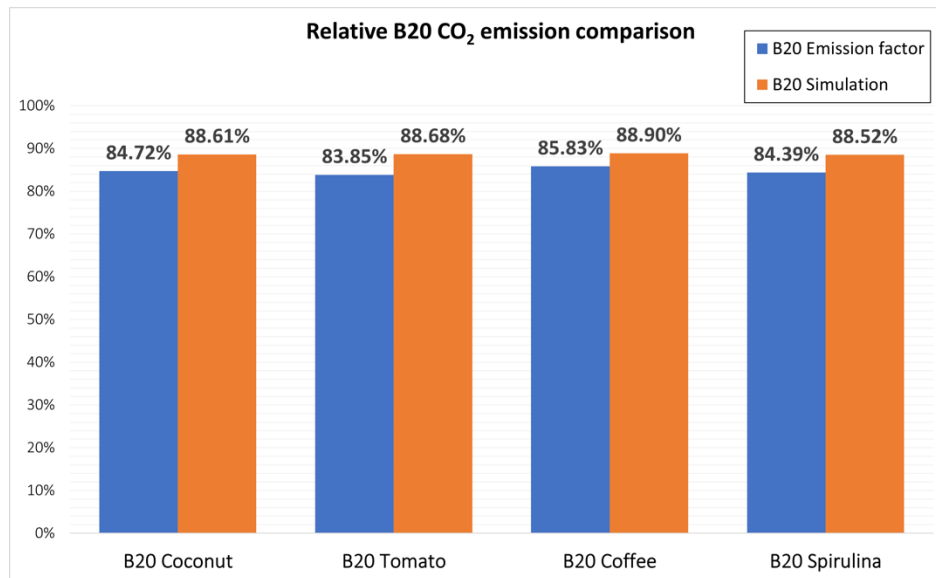
Figure 36 Relative B20 CO$_2$ emission comparison
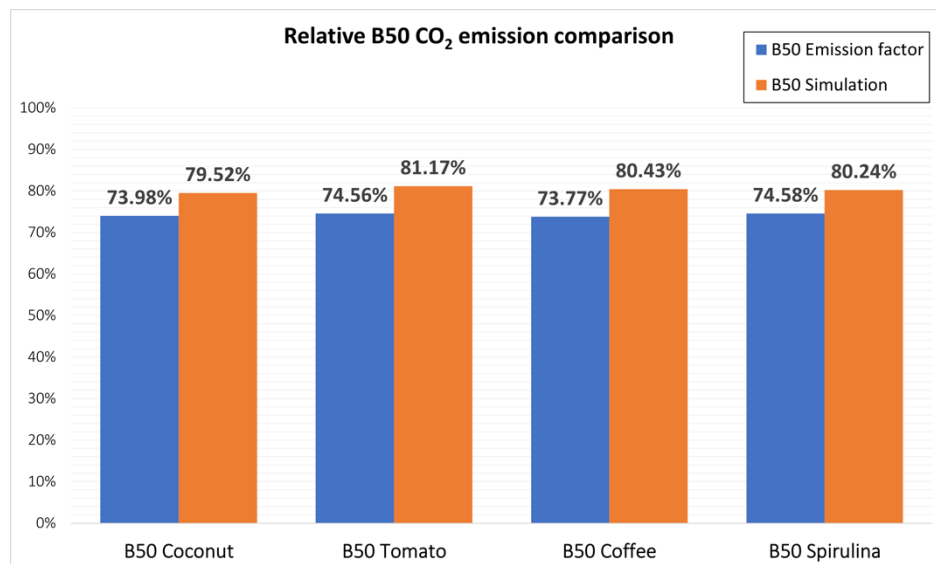
Figure 37 Relative B50 CO$_2$ emission comparison

By calculating CO$_2$ emission using the Emission factor method, slightly higher CO$_2$ reductions are recorded across all the fuel blends. Nevertheless, considering that the two methods showed similar CO$_2$ emissions, the Emission factor approach can give a good approximation for the diesel-biodiesel blends in a short time. However, a CFD analysis of in-cylinder combustion is advised for a more in-depth view of the exhaust gasses composition as many engine parameters can be altered, leading to a very detailed insight into exhaust gasses.

5 CONCLUSION

In this thesis, a CFD combustion analysis using chemical kinetics for different generations of Biodiesel and its blends was performed. Biodiesel, due to its similar physical properties to conventional diesel, is highly applicable in ICE when blended with traditional diesel. Also, being CO_2 neutral makes it an attractive alternative for replacing standard fossil fuels. Four different plant-derived feedstocks in B20 and B50 blends were analyzed in CFD software AVL-FIRE™ in four operating points, where combustion characteristics such as in-cylinder pressure, temperature and rate of heat release were analyzed and compared to experimental data.

A reduced chemical mechanism capable of depicting biodiesel behaviour via two species surrogates was used. The mechanism consisted of 115 species and 460 chemical reactions.

The comparison to the experimental data showed good agreement during the compression and expansion period. However, shorter ignition delay times and slightly higher peak values were obtained in all the operating points, which can be attributed to the fuel being depicted by surrogate species. B20 and B50 biodiesel blends showed lower values for all combustion characteristics when the same amount of fuel was injected. This behaviour was due to lower LHV for Biodiesel, implying that more fuel needs to be injected for reaching the same amounts of released energy per cycle.

A reduction in NO_x was also observed for diesel-biodiesel blends compared to conventional diesel.

For the CO_2 emissions, a comparison between CFD simulations and the Emission factor method was conducted. By calculating the emissions by the Emission factor method, slightly higher CO2 reductions are noted. For large-scale cases, where a quick approximation is needed, the Emission factor can offer a good CO_2 approximation. However, for a more detailed analysis of CO_2 emissions and exhaust gasses in general, CFD simulations can offer a more precise and in-depth analysis of specific fuel emissions.

Concerning the chemical structure of the analyzed feedstock, waste tomato-seed oils have shown to be the best, with good combustion characteristics and reduction in CO_2 and NO_x. Also, it is worth mentioning that second and third-generation biodiesels have an overall positive impact on CO_2 emissions as they are CO_2 neutral. Microalgae biodiesel will be a perfect alternative when it becomes profitable as they have a much shorter harvesting time and a much higher oil content than traditional biodiesel oilseeds.

Finally, it can be stated that combustion analysis using chemical kinetics offers good insight into biodiesel behaviour. With some additional engine parameters optimization and a detailed chemical mechanism where Biodiesel is not depicted by surrogates, better results can be obtained, and diesel-biodiesel blends can match the behaviour of conventional diesel.

References

[1]   Widayat, A.D.K. Wibowo, Hadiyanto, Study on Production Process of Biodiesel from Rubber Seed (Hevea Brasiliensis) by in Situ (Trans)Esterification Method with Acid Catalyst, Energy Procedia. 32 (2013) 64–73. https://doi.org/10.1016/j.egypro.2013.05.009.

[2]   Z. Petranović, T. Bešenić, M. Vujanović, N. Duić, Modelling pollutant emissions in diesel engines, influence of biofuel on pollutant formation, Journal of Environmental Management. 203 (2017) 1038–1046. https://doi.org/10.1016/j.jenvman.2017.03.033.

[3]   J. E, Z. Zhang, J. Chen, M. Pham, X. Zhao, Q. Peng, B. Zhang, Z. Yin, Performance and emission evaluation of a marine diesel engine fueled by water biodiesel-diesel emulsion blends with a fuel additive of a cerium oxide nanoparticle, Energy Conversion and Management. 169 (2018) 194–205. https://doi.org/10.1016/j.enconman.2018.05.073.

[4]   M. Robaina, A. Neves, Complete decomposition analysis of CO2 emissions intensity in the transport sector in Europe, Research in Transportation Economics. 90 (2021) 101074. https://doi.org/10.1016/j.retrec.2021.101074.

[5]   D. Tan, Z. Chen, J. Li, J. Luo, D. Yang, S. Cui, Z. Zhang, Effects of Swirl and Boiling Heat Transfer on the Performance Enhancement and Emission Reduction for a Medium Diesel Engine Fueled with Biodiesel, Processes. 9 (2021) 568. https://doi.org/10.3390/pr9030568.

[6]   H. Stančin, H. Mikulčić, X. Wang, N. Duić, A review on alternative fuels in future energy system, Renewable and Sustainable Energy Reviews. 128 (2020) 109927. https://doi.org/10.1016/j.rser.2020.109927.

[7]   E.G. Giakoumis, C.D. Rakopoulos, A.M. Dimaratos, D.C. Rakopoulos, Exhaust emissions of diesel engines operating under transient conditions with biodiesel fuel blends, Progress in Energy and Combustion Science. 38 (2012) 691–715. https://doi.org/10.1016/j.pecs.2012.05.002.

[8]   J. Sun, J.A. Caton, T.J. Jacobs, Oxides of nitrogen emissions from biodiesel-fuelled diesel engines, Progress in Energy and Combustion Science. 36 (2010) 677–695. https://doi.org/10.1016/j.pecs.2010.02.004.

[9]   B.D. Wahlen, M.R. Morgan, A.T. McCurdy, R.M. Willis, M.D. Morgan, D.J. Dye, B. Bugbee, B.D. Wood, L.C. Seefeldt, Biodiesel from Microalgae, Yeast, and Bacteria: Engine Performance and Exhaust Emissions, Energy & Fuels. 27 (2013) 220–228. https://doi.org/10.1021/ef3012382.

[10]   M.M. Rahman, S. Stevanovic, M.A. Islam, K. Heimann, M.N. Nabi, G. Thomas, B. Feng, R.J. Brown, Z.D. Ristovski, Particle emissions from microalgae biodiesel combustion and their relative oxidative potential, Environmental Science: Processes & Impacts. 17 (2015) 1601–1610. https://doi.org/10.1039/C5EM00125K.

[11]   S.A. Ahmed, S. Zhou, Y. Zhu, Y. Feng, A. Malik, N. Ahmad, Influence of Injection Timing on Performance and Exhaust Emission of CI Engine Fuelled with Butanol-Diesel Using a 1D GT-Power Model, Processes. 7 (2019) 299. https://doi.org/10.3390/pr7050299.

[12]   U. Rajak, P. Nashine, P.K. Chaurasiya, T.N. Verma, D.K. Patel, G. Dwivedi, Experimental & predicative analysis of engine characteristics of various biodiesels, Fuel. 285 (2021) 119097. https://doi.org/10.1016/j.fuel.2020.119097.

[13]   S.R. Amini Niaki, S. Mahdavi, J. Mouallem, Experimental and simulation investigation of effect of biodiesel-diesel blend on performance, combustion, and emission

characteristics of a diesel engine, Environmental Progress & Sustainable Energy. 37 (2018) 1540–1550. https://doi.org/10.1002/ep.12845.

[14]　H. An, W.M. Yang, J. Li, Effects of ethanol addition on biodiesel combustion: A modeling study, Applied Energy. 143 (2015) 176–188. https://doi.org/10.1016/j.apenergy.2015.01.033.

[15]　L. Lešnik, B. Vajda, Z. Žunič, L. Škerget, B. Kegl, The influence of biodiesel fuel on injection characteristics, diesel engine performance, and emission formation, Applied Energy. 111 (2013) 558–570. https://doi.org/10.1016/j.apenergy.2013.05.010.

[16]　Y. Zhang, Y. Zhong, J. Wang, D. Tan, Z. Zhang, D. Yang, Effects of Different Biodiesel-Diesel Blend Fuel on Combustion and Emission Characteristics of a Diesel Engine, Processes. 9 (2021) 1984. https://doi.org/10.3390/pr9111984.

[17]　S. Sukumaran, S.-C. Kong, Modelling biodiesel–diesel spray combustion using multicomponent vaporization coupled with detailed fuel chemistry and soot models, Combustion Theory and Modelling. 20 (2016) 913–940. https://doi.org/10.1080/13647830.2016.1199917.

[18]　M. Costa, M. la Villetta, N. Massarotti, D. Piazzullo, V. Rocco, Numerical analysis of a compression ignition engine powered in the dual-fuel mode with syngas and biodiesel, Energy. 137 (2017) 969–979. https://doi.org/10.1016/j.energy.2017.02.160.

[19]　A. Stagni, C. Saggese, M. Bissoli, A. Cuoci, A. Frassoldati, T. Faravelli, E. Ranzi, Reduced kinetic model of biodiesel fuel combustion, Chemical Engineering Transactions. 37 (2014) 877–882. https://doi.org/10.3303/CET1437147.

[20]　E. Ranzi, A. Frassoldati, A. Stagni, M. Pelucchi, A. Cuoci, T. Faravelli, Reduced Kinetic Schemes of Complex Reaction Systems: Fossil and Biomass-Derived Transportation Fuels, International Journal of Chemical Kinetics. 46 (2014) 512–542. https://doi.org/10.1002/kin.20867.

[21]　L. Zhang, X. Ren, Z. Lan, A reduced reaction mechanism of biodiesel surrogates with low temperature chemistry for multidimensional engine simulation, Combustion and Flame. 212 (2020) 377–387. https://doi.org/10.1016/j.combustflame.2019.11.002.

[22]　Z. Luo, M. Plomer, T. Lu, S. Som, D.E. Longman, S.M. Sarathy, W.J. Pitz, A reduced mechanism for biodiesel surrogates for compression ignition engine applications, Fuel. 99 (2012) 143–153. https://doi.org/10.1016/j.fuel.2012.04.028.

[23]　J.L. Brakora, Y. Ra, R.D. Reitz, Combustion Model for Biodiesel-Fueled Engine Simulations using Realistic Chemistry and Physical Properties, SAE International Journal of Engines. 4 (2011) 2011-01–0831. https://doi.org/10.4271/2011-01-0831.

[24]　K. Hanjalić, M. Popovac, M. Hadžiabdić, A robust near-wall elliptic-relaxation eddy-viscosity turbulence model for CFD, International Journal of Heat and Fluid Flow. 25 (2004) 1047–1051. https://doi.org/10.1016/j.ijheatfluidflow.2004.07.005.

[25]　M. Vujanović, Numerical modelling of multiphase flow in combustion of liquid fuel, Sveučilište u Zagrebu Fakultet strojarstva i brodogradnje, 2010. https://urn.nsk.hr/urn:nbn:hr:235:036060.

[26]　AVL List GmbH, AVL FIRE Spray User Manual, (2021).

[27]　A. Aissa, M. Abdelouahab, A. Noureddine, M. Elganaoui, B. Pateyron, Ranz and Marshall correlations limits on heat flow between a sphere and its surrounding gas at high temperature, Thermal Science. 19 (2015) 1521–1528. https://doi.org/10.2298/TSCI120912090A.

[28]　AVL List GmbH, AVL FIRE General Gas Phase Reactions Module User Manual, (2021).

[29]　Z. Petranović, Numerical modelling of spray and combustion processes using the Euler Eulerian multiphase approach, Sveučilište u Zagrebu, Fakultet strojarstva i brodogradnje, 2016. https://urn.nsk.hr/urn:nbn:hr:235:810384.

[30] H.J. Curran, P. Gaffuri, W.J. Pitz, C.K. Westbrook, A Comprehensive Modeling Study of n-Heptane Oxidation, Combustion and Flame. 114 (1998) 149–177. https://doi.org/10.1016/S0010-2180(97)00282-4.

[31] O. Herbinet, W.J. Pitz, C.K. Westbrook, Detailed chemical kinetic mechanism for the oxidation of biodiesel fuels blend surrogate, Combustion and Flame. 157 (2010) 893–908. https://doi.org/10.1016/j.combustflame.2009.10.013.

[32] F. Ma, M.A. Hanna, Biodiesel production: a review1Journal Series #12109, Agricultural Research Division, Institute of Agriculture and Natural Resources, University of Nebraska–Lincoln.1, Bioresource Technology. 70 (1999) 1–15. https://doi.org/10.1016/S0960-8524(99)00025-5.

[33] S. Pinzi, P. Rounce, J.M. Herreros, A. Tsolakis, M. Pilar Dorado, The effect of biodiesel fatty acid composition on combustion and diesel engine exhaust emissions, Fuel. 104 (2013) 170–182. https://doi.org/10.1016/j.fuel.2012.08.056.

[34] S.K. Hoekman, A. Broch, C. Robbins, E. Ceniceros, M. Natarajan, Review of biodiesel composition, properties, and specifications, Renewable and Sustainable Energy Reviews. 16 (2012) 143–169. https://doi.org/10.1016/j.rser.2011.07.143.

[35] R. Karami, M.G. Rasul, M.M.K. Khan, M. Mahdi Salahi, M. Anwar, Experimental and computational analysis of combustion characteristics of a diesel engine fueled with diesel-tomato seed oil biodiesel blends, Fuel. 285 (2021) 119243. https://doi.org/10.1016/j.fuel.2020.119243.

[36] A. Sander, A. Petračić, J. Parlov Vuković, L. Husinec, From Coffee to Biodiesel—Deep Eutectic Solvents for Feedstock and Biodiesel Purification, Separations. 7 (2020) 22. https://doi.org/10.3390/separations7020022.

[37] U. Rajak, P. Nashine, T.N. Verma, Assessment of diesel engine performance using spirulina microalgae biodiesel, Energy. 166 (2019) 1025–1036. https://doi.org/10.1016/j.energy.2018.10.098.

[38] A. Demirbaş, Fuel properties and calculation of higher heating values of vegetable oils, Fuel. 77 (1998) 1117–1120. https://doi.org/10.1016/S0016-2361(97)00289-5.

[39] M.S. Shehata, Emissions, performance and cylinder pressure of diesel engine fuelled by biodiesel fuel, Fuel. 112 (2013) 513–522. https://doi.org/10.1016/j.fuel.2013.02.056.

[40] G.A. Marrero, J. Rodríguez-López, R.M. González, Car usage, CO2 emissions and fuel taxes in Europe, SERIEs. 11 (2020) 203–241. https://doi.org/10.1007/s13209-019-00210-3.